

PARTICLE SIMULATION OF ELECTROMAGNETIC WAVES  
AND  
ITS APPLICATION TO SPACE PLASMAS

Hiroshi Matsumoto and Yoshiharu Omura

Radio Atmospheric Science Center,  
Kyoto University,  
Uji, Kyoto 611, Japan

ABSTRACT

In this article, we present a basic description of particle simulation codes developed at RASC of Kyoto University for the study of wave phenomena in space plasmas. Out of the available codes at RASC, two most-frequently-used codes are presented here. One of them is the full electromagnetic code named KEMPO (Kyoto University ElectroMagnetic Code) which is able to treat both electromagnetic and electrostatic wave modes simultaneously with a special time-filter technique using a multi-time-step (MTS) scheme. The other is the long time scale code (LTS) named KULTS (Kyoto University LTS ) which is useful for studies of whistler mode wave-particle interactions over hundreds to thousands of wavelengths in both homogeneous and inhomogeneous plasmas. Principles and basic techniques of the codes as well as examples of their applications to space plasma problems are presented.

1. INTRODUCTION

Space exploration has been achieved by a rapid development of space vehicles and their use for scientific survey of our space environment. In 1960's and 1970's, lots of discoveries of new space phenomena were brought back from these spacecraft observations. Data analysis-phase followed after the discovery-phase yielding a variety of physical models of our space plasma environment and theories for the related plasma processes taking place therein. However, there still remains a large number of problems because of too many degrees of freedom of choice of physical models. Natural phenomena in space plasmas are often highly nonlinear and too complicated for theories which usually rely on linearity or weak nonlinearity, symmetry

characteristics, homogeneity or simple inhomogeneity and other simplistic assumptions. On the other hand, experiments by satellite observations are still too coarse: Measurements are limited in time and in space leaving a large amount of ambiguity and disputes among researchers as to the interpretation of the observed results and related theoretical models. To resolve these uncertainties among various models and theories and to find a hint or clue for understanding the unsolved physics underlying the observed phenomena, computer simulations have been highlighted as a third promising research approach by bridging the traditional two approaches, theory and experiment, among space researchers in late 1970's and in 1980's.

Computer simulations for space physics may be divided into two categories: First is an MHD simulation which follows the nonlinear fluid motion of plasmas in their self-consistent fields (and applied fields if any). This class of simulations is useful in understanding macroscopic global-scale dynamics which cannot be understood by piecewise information from individual satellite observations. Second is a particle simulation which follows the nonlinear motion of many particles in their self-consistent fields (and applied fields if any). Particle simulations play a significant role in space physics in interpreting highly nonlinear kinetic effects like wave instabilities and associated plasma scattering, diffusion, heating and particle acceleration. Complicated and sometimes overlapping phenomena which nature generally exhibits can be decomposed into simpler elements of physics in simulations to obtain a clearer physical picture. One of the advantages of the computer simulation is that one can make as detailed diagnostics of plasma and field quantities as one desires. A precise visualization of the time evolution of the nonlinear micro-dynamics of interest is easily achieved in detail by graphic displays of the results of particle simulations. This could not be realized either by theory nor by satellite observations. Thus particle simulations provide useful data of wave-particle interactions which are inaccessible to satellite observations nor to theories. One such example is the rapid variation of the particle distribution function in velocity space. Such detailed information may often provide a hint and inspiration not only for further theoretical development but also for design of new satellite observations.

In this article, we will give an introductory review and guide of particle simulation of electromagnetic waves in plasmas and its application to space plasma phenomena. Basic concept of particle simulations is not given in detail because it is described elsewhere in this book [Okuda], and is found in the existing literature [e.g., Langdon and Lasinski, 1976; Hockney and Eastwood, 1981; Birdsall and Langdon, 1984]. Application to electrostatic wave phenomena is not presented either for the same reason. Two different codes are explained in this article which our research group have so far developed for the studies of electromagnetic wave phenomena in space. They are (1) Full Electromagnetic (FEM) code, and (2) Long Time Scale (LTS) code. These computer codes developed at Kyoto University are

named "KEMPO" (Kyoto University ElectroMagnetic Particle cOde) and "KULTS" (Kyoto University LTS code), respectively.

In section 2, we briefly introduce a tutorial model and concepts of particle simulations for electromagnetic wave phenomena. Section 3 and 4 are devoted to the description of the basic equations and elements for coding of the KEMPO and KULTS, respectively. Development of the diagnostic tools is as important as coding of main programs in order to display various information in different ways so that one can extract meaningful physical results and can construct improved models and refine the related theory. Section 5 presents an outline of the diagnostic tools used in the KEMPO and KULTS particle codes. In section 6, applications of these codes to electromagnetic wave phenomena in space plasmas are presented.

## 2. ELEMENTARY CONCEPTS AND MODELS IN PARTICLE SIMULATIONS

In this section, we will give a short review of basic concept and models used in particle simulation in general. Readers are recommended to refer to existing textbook and literature for details [Morse and Nielson, 1969; Birdsall and Fuss, 1969; Dawson, 1970; Birdsall, Langdon and Okuda, 1970; Hockney, 1970; Langdon and Birdsall, 1970; Okuda and Birdsall, 1970; Okuda and Dawson, 1973; Langdon and Lasinski, 1976; Nielson and Lewis, 1976; Hockney and Eastwood, 1981; Birdsall and Langdon, 1984].

### 2.1 Superparticles

In particle simulation, plasma dynamics is studied by following a large number of particles in their self-consistent electric and magnetic fields. Naturally, one cannot emulate nature even with the today's super-computer. Only several orders of magnitude less number of particles are treatable in computer compared with the enormous number of particles in the real plasma of almost any size of interest. Therefore we are obliged to use an artificial model-particle called "superparticle" with a larger mass and charge than the real particle. The superparticle represents many particles in a real plasma, and has a finite size with its charge being distributed over a finite region of space.

The concept of the finite-sized superparticle was introduced historically by two research groups. First one was "Cloud-in-Cell(CIC)" [Birdsall and Fuss, 1969] and the other was "Particle-in-Cell(PIC)" [Morse and Nielson, 1969]. Both were introduced as an improved model of zero-sized superparticle (plasma sheet mode) to suppress statistical fluctuations and short range collisions caused by a delta-functional nature of the zero-sized superparticles [Hockney, 1966; Birdsall and Fuss, 1969; Morse and Nielson, 1969; Okuda and Birdsall, 1970; Langdon and Birdsall, 1970]. At the same time the method of assignment of charge and current of the superparticle to its

neighboring spatial grids was improved from NGP (Nearest Grid Point) scheme to AS (Area Sharing) scheme [Morse and Nielson, 1969], MPE (Multipole Expansion) scheme and SUDS (Subtracted Dipole Scheme) [Kruer et al., 1973]. The theoretical works were developed on the modification of the plasma theory for the finite-size superparticle plasma [Langdon and Birdsall, 1970; Okuda and Birdsall, 1970]. Details such as modification of the dispersion characteristics and of the collisional effects are discussed elsewhere in this book [Okuda] and are not given here.

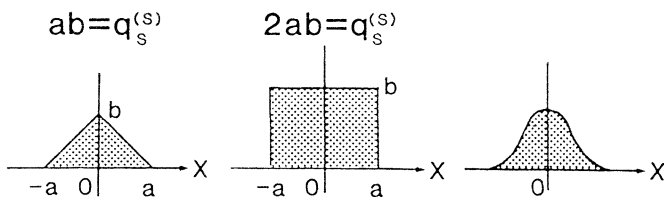


Figure 1. Three shapes of superparticle: (1) Square-shaped, (2) Triangular-shaped, (3) Gaussian-shaped.

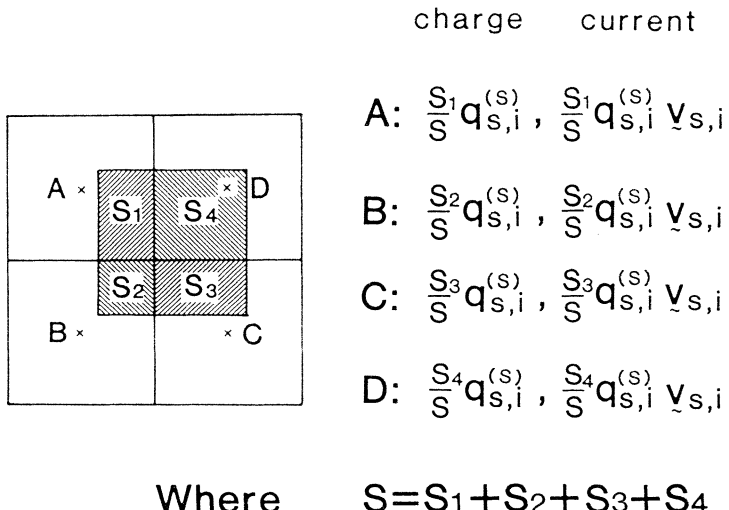


Figure 2. Schematic illustration of charge and current assignment for the square-shaped superparticle.

The shape of the superparticle can be of any form. Normally, however, one of the following three shapes is, for practical codings, hired in the particle simulation. These three shapes for one dimensional case are depicted in Figure 1. They are (1) Square-shaped, (2) Triangular-shaped, and (3) Gaussian-shaped. As for the scheme for the charge and current assignment to the neighboring grid points, the AS (area sharing) scheme is most frequently used. A schematic illustration of charge and current assignment for the square-shaped superparticle is given in Figure 2. In the figure the size of the square-shaped superparticle is assumed to be identical to that of the grid (or cell). Charge and current of a superparticle is shared by grid points where the superparticle is located. The charge and current assignment is made in such a way that the share to each grid is proportional to the overlapped area of that of the superparticle and the cell area of the grid. Other methods of the charge and current assignment have been proposed and are described in the literature [e.g., Hockney and Eastwood, 1981; Birdsall and Langdon, 1984; Okuda, 1984].

The charge and mass of the superparticle is much larger than those of the real particle. However the following three densities of the superparticles are kept the same as those of the real particles.

#### (1) Charge Density

$$N_S Q_S = N_r Q_r \quad (1)$$

#### (2) Mass Density

$$N_S M_S = N_r M_r \quad (2)$$

#### (3) Energy Density

$$N_S \kappa T_S = N_r \kappa T_r \quad (3)$$

where the suffixes, s and r, mean the quantities of the super- and real-particles, and  $N$ ,  $Q$ ,  $M$ ,  $\kappa$  and  $T$  denote number density, charge, mass, Boltzmann's constant and temperature, respectively. Under these equalities, not only the charge to mass ratio but also the basic physical quantities such as the plasma and cyclotron frequencies, the Debye length, and the thermal velocity are kept identical to each other in both simulational and real plasmas. Thus the most of the physical properties of the plasma are reproduced in the particle simulation.

## 2.2 Discretization of Space and Time

In the particle simulation, both space and time are discretized. Spatial discretization is introduced by two reasons. One is to speed up the calculation of force acting on particles [Buneman, 1959; Dawson, 1961]. Instead of calculating all contribution of Coulomb force from all particles, the force acting on a superparticle is calculated by field quantities defined on the grid points nearby the

particle. Second reason is that the superparticle has a finite size over a certain region of space so that the spatial resolution smaller than the particle size is unnecessary and meaningless. Normally, the spatial grid spacing is taken to be from 1 to 3 times the Debye length. Numerical stability related to the choice of the grid size has been studied in detail and is found in the literature [Langdon and Birdsall, 1970; Okuda, 1970; Abe et al., 1975].

Time discretization is inevitable in any numerical approach to any partial differential equations. The problem is how large we can choose the time step keeping the numerical stability. To avoid the numerical instability, the Courant-Friedrichs-Lowy (CFL) condition should be satisfied. In case of the electromagnetic particle simulation, the CFL condition is

$$\Delta t < \Delta r / (c/n) \quad (4)$$

where  $n$  is the spatial dimension of the model, and  $c$  is the light speed.

Discretization of space and time modifies the dispersion characteristics. This modification comes from digital samplings of continuous quantities in space and time. As is well known from the sampling theorem, the frequency  $\omega$  and wavenumber  $k$  should be replaced by  $\Omega = \sin(\omega\Delta t/2)/(\omega\Delta t/2)$  and  $K = \sin(k\Delta r/2)/(k\Delta r/2)$ , respectively. Thus the dispersion equation for real plasma,  $D(\omega, k) = 0$  is modified to  $D(\Omega, K) = 0$ . Because of this sampling function nature, high frequency and large  $k$  components are folded down in the low and small  $k$  domain in the  $\omega$ - $k$  space as "aliases". This effect should always be taken into account both in designing the model of simulation and in analyzing the simulation data.

### 2.3 Average Field and Self-Force

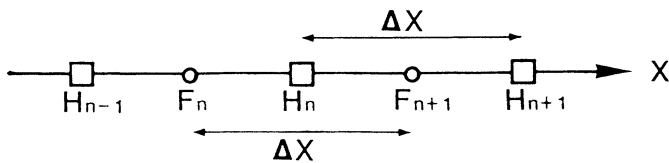
Since the charge of the superparticle with a finite size smears out in space, the force acting on it is the average one. In this subsection, we will discuss the procedure for the average and its related self-force problem. To this purpose, we will confine ourselves only to the simplest case of the square-shaped superparticle in one-dimensional case. Extension to the case of superparticles with other shapes and/or two-dimensional case is straightforward. We also limit our discussion only to the case of the electrostatic electric field as an example of the self-force. The magnetostatic self-force can be treated in a similar manner.

To guarantee the centered difference scheme for Maxwell's equation (Poisson's equation in this particular example), we normally adopt a staggered dual grid system composed of full-integer- and half-integer grid points as illustrated in Figure 3(a). The open circle points indicate full-integer-grid points on which the charge is defined. The open square symbols along the  $x$ -axis are half-integer grid points on which the electric field  $E_x$  is defined. Suppose that a superparticle with a size of the grid spacing  $\Delta x$  is located at point P

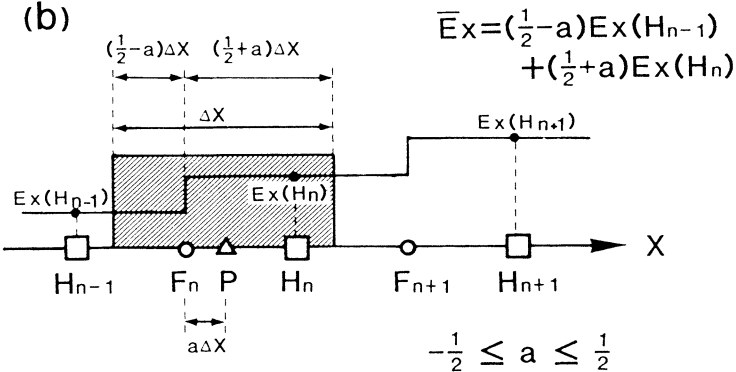
in between  $F_n$  and  $F_{n+1}$  with a distance  $a\Delta X$  from  $F_n$  as illustrated in Figure 3(b). Then the weighted average of the electric field  $\bar{E}$  is given by

(a)

- Full Integer Grid Points for  $\rho$
- Half Integer Grid Points for  $E_x$



(b)



(C)

$$Ex = Ex^{INT} = (\frac{1}{2}-a)Ex(H_{n-1}) + (\frac{1}{2}+a)Ex(H_n)$$

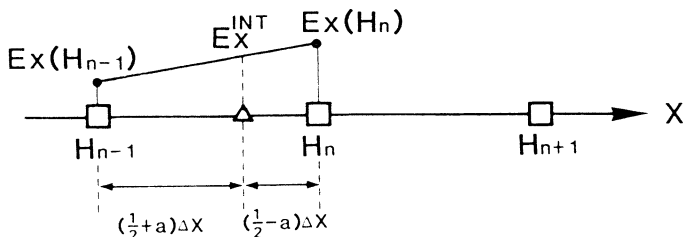
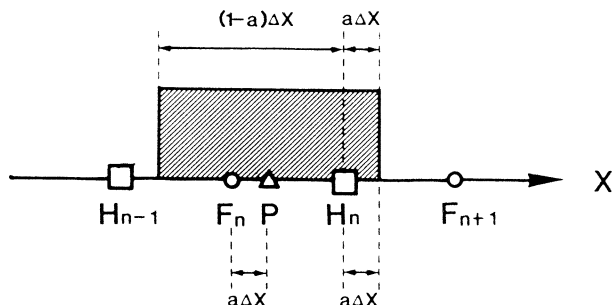


Figure 3. Staggered dual grid system and effective electric field acting on a superparticle.

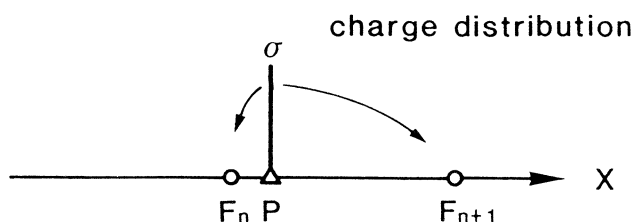
$$\bar{E} = \left( \frac{1}{2} - a \right) E_X(H_{n-1}) + \left( \frac{1}{2} + a \right) E_X(H_n). \quad (5)$$

The effective electric field which the superparticle feels is this averaged value  $\bar{E}$ . It is formally computed by a simple linear interpolation from two values of  $E_X$  at two adjacent grid points  $H_{n-1}$  and  $H_n$  as shown in Figure 3(c). However, one should note that the simple interpolated value  $E^{INT}(P)$  from  $E_X(H_{n-1})$  and  $E_X(H_n)$  produces a nonphysical force acting on the superparticle. The nonphysical force

(a)



(b)



(C)

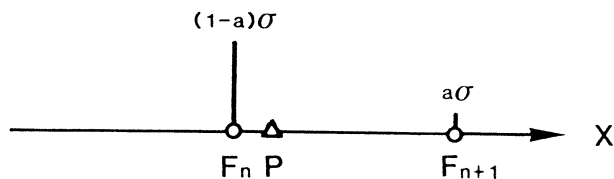


Figure 4. Charge distribution of superparticles to grid points.

is called a "self-force". Physically, the electric or magnetic field produced by a particle should not give any force back to the particle itself.

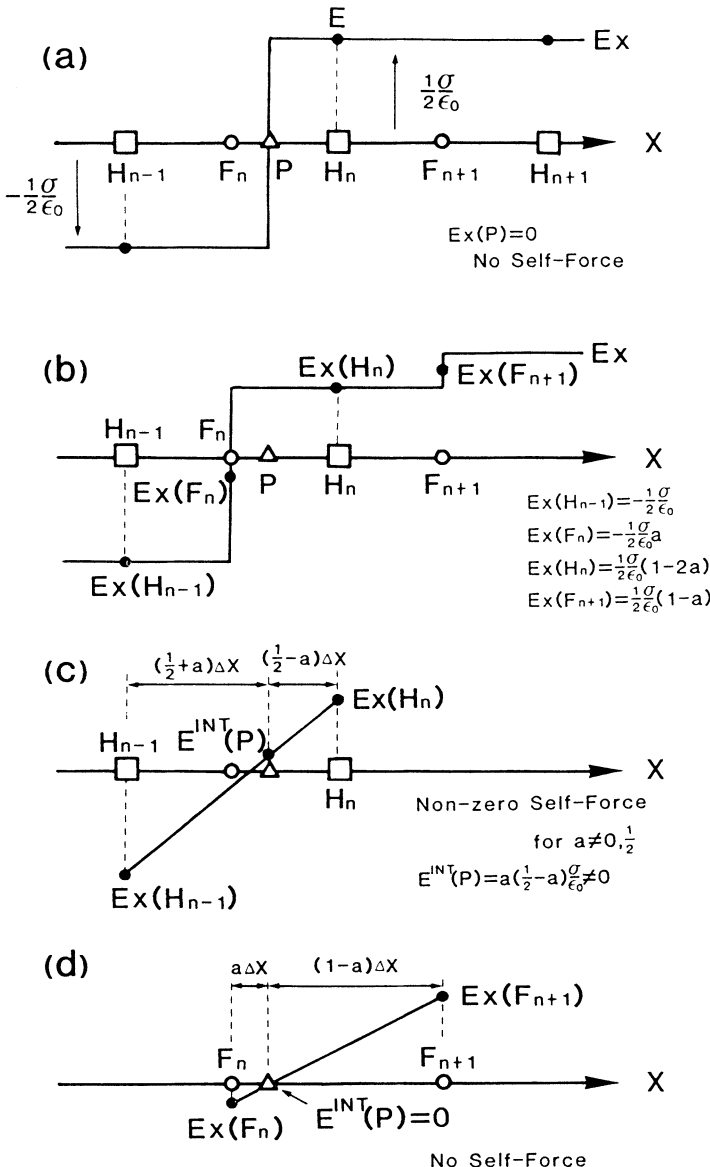


Figure 5. Explanation of self-force and its cancellation.

As far as we adopt the staggered dual grid system together with the area sharing scheme for charge and current distribution to grid points, the self-force comes in automatically and leads to violation of conservation of energy and momentum by the nonphysical acceleration of particles. To demonstrate how the self-force appears, let us consider a case where only one superparticle is placed in the system at point P as shown in Figure 4(a). The charge density  $\sigma$  of the superparticle is distributed to two adjacent grid points  $F_n$  and  $F_{n+1}$  by the area sharing scheme. This process is identical to divide the concentrated charge density  $\sigma$  at the point P onto  $F_n$  and  $F_{n+1}$  as illustrated in Figure 4(b). The resultant charges at  $F_n$  and  $F_{n+1}$  are  $(1-a)\sigma$  and  $a\sigma$ , respectively as shown in Figure 4(c). The electrostatic field  $E_x$  produced by the particle is presented by a step function with a jump of amount of  $\sigma/\epsilon_0$  as shown in Figure 5(a). Due to the symmetry characteristics,  $E_x = 0$  at the particle location P. However, in the computer simulation, the electric fields at half-integer grid points are calculated from the charge distribution at full-integer grid points. Thus as illustrated in Figure 5(b), the electric field at the half-integer points are

$$\begin{aligned} E_x(F_{n+1}) &= -\frac{1}{2} \frac{\sigma}{\epsilon_0} \\ E_x(F_n) &= \frac{1}{2} \frac{\sigma}{\epsilon_0} (1 - 2a) \end{aligned} \quad (6)$$

These values are, in turn, used to compute the effective electric field acting on the superparticle at P using Eq.(5). Then, unfortunately, the result is given by

$$\bar{E}_x(P) = E_x^{\text{INT}}(P) = a(\frac{1}{2} - a) \frac{\sigma}{\epsilon_0} \quad (7)$$

which is not zero except for special cases of  $a = 0$  or  $1/2$  as illustrated by Figure 5(c). This non-zero electric field acts on the particle and accelerates it nonphysically. Therefore, we cannot simply estimate the effective electric fields by Eq.(5) if we use the  $E_x$  values at half-integer points. However, as shown in Figure 5(d), the correct value can be computed by the same linear interpolation scheme if we use the electric field values at  $F_n$  and  $F_{n+1}$ , i.e., at two adjacent full-integer points. The values of  $E_x$  at these full-integer points are given by (see Figure 5(b))

$$\begin{aligned} E_x(F_n) &= -\frac{1}{2} \frac{\sigma}{\epsilon_0} a \\ E_x(F_{n+1}) &= \frac{1}{2} \frac{\sigma}{\epsilon_0} (1 - a) \end{aligned} \quad (8)$$

which yields

$$\bar{E}_x(P) = E_x^{\text{INT}}(P) = 0 \quad (9)$$

Therefore, to avoid the self-force, we need to relocate the values of

$E_x$  onto the same grid points where the charge is defined. In the same way, the magnetic field should be relocated onto the grid points where the current is defined. Details of the grid assignment of various physical quantities are described in Section 3.3.

### 3. PARTICLE CODE VALID FOR BOTH ELECTROMAGNETIC AND ELECTROSTATIC WAVE MODELS

#### 3.1 General Features of EM2 Code (KEMPO)

We have developed a two-and-a-half dimensional electromagnetic simulation code which solves Maxwell's equations and equations of motion of electrons and, if necessary, ions explicitly. We assume  $(x, y, z)$ -coordinates neglecting variation along the  $z$  axis, i.e.,  $\partial/\partial z = 0$ . Three velocity components  $v_x, v_y, v_z$  and all three components of electromagnetic fields  $E$  and  $B$  are retained. Since no approximation is made to the basic equations except for  $\partial/\partial z = 0$ , the code is applicable to a wide range of two-dimensional problems in plasma physics. The algorithm for integration of the field and particles is designed basically after Langdon and Lasinski [1976]. The fields are integrated using Maxwell's equations in a central difference form in space and time. Particles are integrated by the Buneman-Boris method [Buneman, 1967; Boris, 1970] which is accurate to the second order and time-reversible. The current density  $J$  and the charge density  $\rho$  are calculated using PIC (particle in cell) method which distributes the current and charge of a superparticle to the adjacent four grid points with area weightings. The electric and magnetic fields acting on a superparticle are interpolated to the particle position from the adjacent four grid points with the same area weightings.

In the following sections we describe several techniques we applied in order to make the simulation code more efficient and accurate. Especially, an Multiple-Time-Step (MTS) scheme we developed makes the code as efficient as the magnetostatic simulation code (with Darwin approximation), and makes it more applicable to low frequency problems of lower hybrid resonance region and of ion wave modes.

#### 3.2 Multiple Time Step Scheme

The time step which satisfies the CFL condition is often too small for the wave modes of interest. Usually the wave frequencies of interest are of the order of the plasma frequency or the cyclotron frequency, while the maximum frequency in the system is  $\pi/\Delta t$ , and much higher than these wave frequencies of interest. Since most of the CPU time is used to solve the particle motion rather than the field integration, it is desired to take a larger time step for the particle calculations. Langdon and Lasinski [1976] proposed an algorithm in which the fields are integrated twice as often as the particles. However, they discovered that the algorithm can lead to a numerical instability. We developed a new algorithm where the particles are

advanced less often than the field without leading to the numerical instability. A filtering of the field quantities in time is performed to avoid the numerical instability.

The high frequency parts of the fast extraordinary (FE) and ordinary (O) modes, i.e., the light modes, receive little contribution from the particle motion which is expressed as the conduction current density  $J$  in Maxwell's equations. This is justified by taking the ratio of the conduction current  $J$  and the displacement current  $\epsilon_0 \partial E / \partial t$

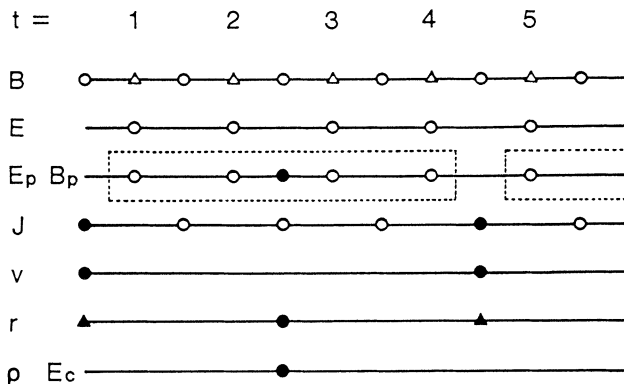
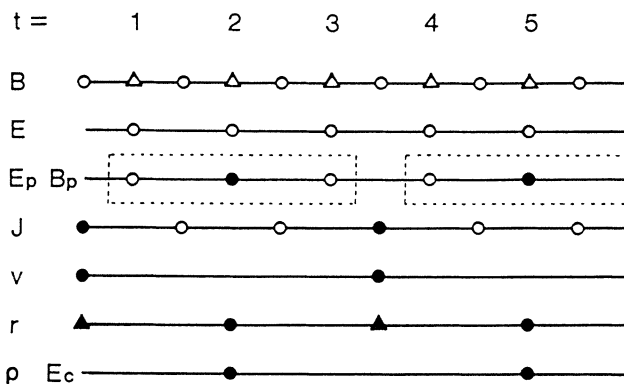
$$\frac{J}{\epsilon_0 \partial E / \partial t} \leq (\frac{\omega_p}{\omega})^2 (1 + \frac{v_{th} B_0}{v_p B_w}) \quad (10)$$

where  $v_{th}$  is the thermal velocity of the particles, and  $v_p$  is the phase velocity of the wave.  $B_w$  is a wave amplitude and  $B_0$  is a static magnetic field. If  $\omega \gg \omega_p$  and  $v_{th}/v_p \leq B_w/B_0$ , the conduction current is negligibly small.

As the particle motion has little effects on the high frequency waves, we may eliminate the high frequency components of the current  $J$ , and treat the high frequency waves as the light mode in vacua. Then velocities and positions of particles may not necessarily be updated at as small time step as in the case of the wave integration. We adopt two different time steps for the field integration and particle integration, respectively. The time step for the field is called "field-time-step" and the time step for the particles is called "particle-time-step". We define the field-time-step as  $\Delta t$  and take the particle-time-step as an integer multiple of the field-time-step, i.e.,  $m\Delta t$ . We call the algorithm using the particle-time-step of  $m\Delta t$  as "Multiple Time Step (MTS) scheme" hereafter.

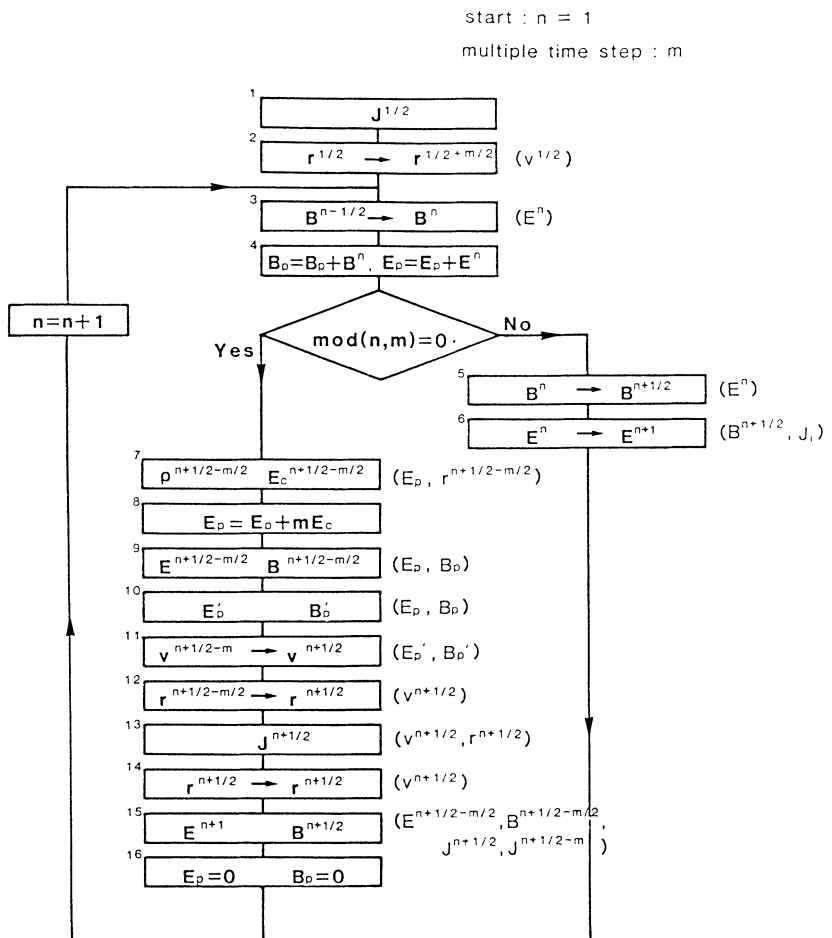
In order to eliminate the high frequency component of the current density  $J$  it is necessary to perform time-filtering of the electromagnetic force acting on the particles. If the particles are not affected by the high frequency electromagnetic force, the conduction current density  $J$ , which is the summation of the particle motion, does not have high frequency components, yielding a consistent simulation. Since the current density  $J$  is calculated at each particle-time-step, the current density at each field-time-step is extrapolated and/or interpolated from the values available at the two nearest particle-time-steps.

In Figure 6 the algorithm of the MTS scheme is depicted as a time step chart. The time step charts are depicted for the case of  $m = [\text{even number}]$  in Figure 6(a) and for the case of  $m = [\text{odd number}]$  in Figure 6(b), respectively.  $E_p$  and  $B_p$  are electric and magnetic fields for particle pushing, which are the sums of the fields  $E$  and  $B$  at the  $m$  time steps indicated by the dashed rectangle in Figure 6. This operation automatically gives averages of the field  $E$  and  $B$  over the period of  $m\Delta t$ , and has an effect of the time filtering, which suppresses the high frequency components of the fields. These

(a)  $m = 4$ (b)  $m = 3$ Figure 6. Time step chart of the MTS scheme : (a)  $m = 4$  (b)  $m = 3$ 

operations are depicted in the flow chart of the KEMPO as illustrated in Figure 7. Using these  $E_p$  and  $B_p$ , we advance the velocities of particles over the particle-time-step  $m\Delta t$ . The fields  $E$  and  $B$  are re-integrated from these  $E_p$  and  $B_p$  over the period  $(m-1)\Delta t/2$  using the field-time-step  $\Delta t$  recursively. The current density  $J$  for the re-integration is interpolated in time from the values at the adjacent particle-time-steps. Then the fields  $E$  and  $B$  are integrated further over the period of  $m\Delta t$  in order to obtain new  $E_p$  and  $B_p$ , where the current density  $J$  is extrapolated from the values at the previous two particle-time-steps.

The MTS scheme has an effect of digital filtering of the electromagnetic fields in time sequence. The digital filtering is  $m$ -point filtering with equal weightings, which is defined by the following equation.



$$J_i = J^{m \cdot [n/m] + 1/2} + \frac{\text{mod}(n,m)}{m} (J^{m \cdot [n/m] + 1/2} - J^{m \cdot [n/m] + 1/2-m})$$

Figure 7. Flow chart of the KEMPO : Quantities in boxes are calculated or advanced in time using quantities in parentheses.

$$\phi_f(T_j) = \frac{1}{m} \sum_{k=-(m-1)/2}^{(m-1)/2} \phi(T_{j+k}) \quad (11)$$

High frequency waves are attenuated at every particle-time-step. The attenuation factor  $A$  of the wave of a frequency  $\omega$  is obtained by assuming

$$\phi(\omega) = \frac{1}{N} \sum_{j=1}^N \phi(T_j) e^{i\omega T_j} \quad (12)$$

where  $N$  is a number of time steps. From (11) and (12), we have

$$\phi_f(\omega) = \frac{1}{m} \sum_{k=-(m-1)/2}^{(m-1)/2} e^{-i\omega(k\Delta t)} \phi(\omega) \quad (13)$$

which gives the attenuation factor for  $m = (\text{even number})$  as

$$A(\omega\Delta t) = \frac{\phi_f(\omega)}{\phi(\omega)} = \frac{2}{m} \left[ \sum_{k=1}^{m/2} \cos \left\{ \left( k - \frac{1}{2} \right) \omega\Delta t \right\} \right] \quad (14)$$

and for  $m = (\text{odd number})$  as

$$A(\omega\Delta t) = \frac{\phi_f(\omega)}{\phi(\omega)} = \frac{1}{m} \left\{ 1 + 2 \sum_{k=1}^{(m-1)/2} \cos(\omega k\Delta t) \right\}. \quad (15)$$

The attenuation factor  $A$  is plotted as a function of  $\omega\Delta t$  for  $m = 2$  to 8 in Figure 8. Since maximum frequency of the system is  $\pi/\Delta t$ ,  $A$  is calculated in the range of  $0 \leq \omega\Delta t \leq \pi$ . As noted from the plot, high frequency modes undergo phase-reversal in the MTS scheme, but they also get damped and disappear from the system.

Electrons undergo oscillation with the plasma frequency  $\omega_p$  in the direction of the static magnetic field. Since the plasma oscillation is a simple harmonic oscillation, the stability criterion for the leapfrog harmonic oscillator [Hockney and Eastwood, 1981] must be satisfied as

$$\omega_p m \Delta t \leq 2. \quad (16)$$

In the transverse plane electrons follow the cyclotron motion with cyclotron frequency  $\omega_c$ . The Buneman-Boris method for particle integration is unconditionally stable for the cyclotron motion. However, if the frequency of the waves of interest are less than or nearly equal to  $\omega_p$  or  $\omega_c$ , the following condition is generally satisfied in order to obtain a reasonable resolution and accuracy.

$$\text{Max}(\omega_p, \omega_c) \cdot m \Delta t \leq 0.2 \quad (17)$$

We define an attenuation rate  $\Gamma_A$  by  $\log A(\omega) / (m\Delta t)$ . In Figure 9 the ratio of the attenuation rate and a wave frequency  $\Gamma_A/\omega$  is plotted as a function of  $\omega\Delta t$  for  $m=1\sim 8$ . The MTS factor  $m$  and field-time-step  $\Delta t$  must be chosen so that  $\Gamma_A$  is much less than physical growth/damping rate of electromagnetic waves in a simulation model.

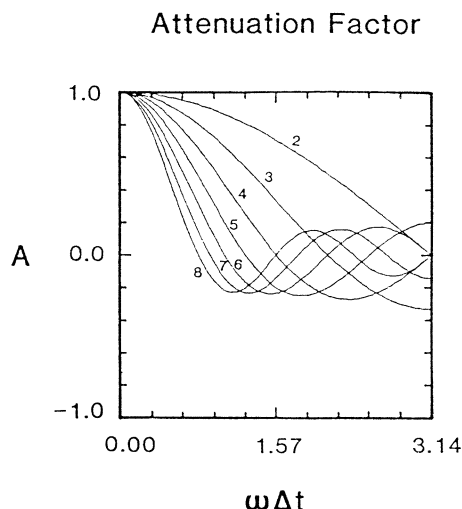


Figure 8. Attenuation factor  $A(\omega\Delta t)$  of the MTS scheme for different multiple time steps.

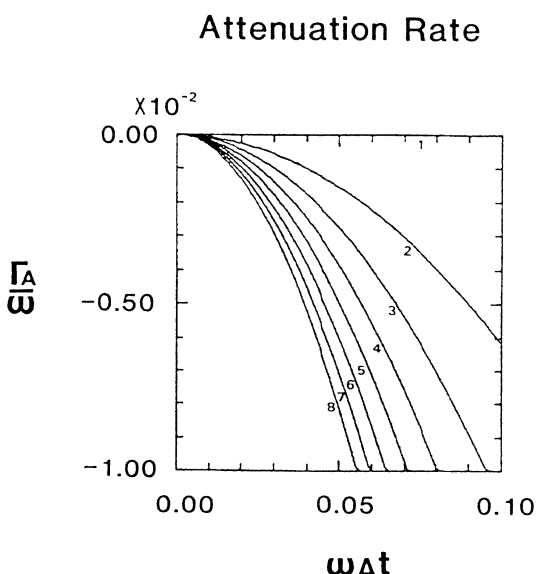


Figure 9. Attenuation rate  $\Gamma_A/\omega$  of the MTS scheme for different multiple time steps.

### 3.3 Grid Location for Integration of the Field

For the two dimensional system Maxwell's equations are reduced to the following two independent sets of equations.

(A)

$$\frac{\partial B_Z}{\partial t} = - \frac{\partial E_y}{\partial x} + \frac{\partial E_x}{\partial y} \quad (18)$$

$$\frac{\partial E_x}{\partial t} = c^2 \left[ \frac{\partial B_Z}{\partial y} - \mu_0 J_x \right] \quad (19)$$

$$\frac{\partial E_y}{\partial t} = c^2 \left[ - \frac{\partial B_Z}{\partial x} - \mu_0 J_y \right] \quad (20)$$

(B)

$$\frac{\partial B_X}{\partial t} = - \frac{\partial E_Z}{\partial y} \quad (21)$$

$$\frac{\partial B_Y}{\partial t} = \frac{\partial E_Z}{\partial x} \quad (22)$$

$$\frac{\partial E_Z}{\partial t} = c^2 \left[ \frac{\partial B_Y}{\partial x} - \frac{\partial B_X}{\partial y} - \mu_0 J_Z \right] \quad (23)$$

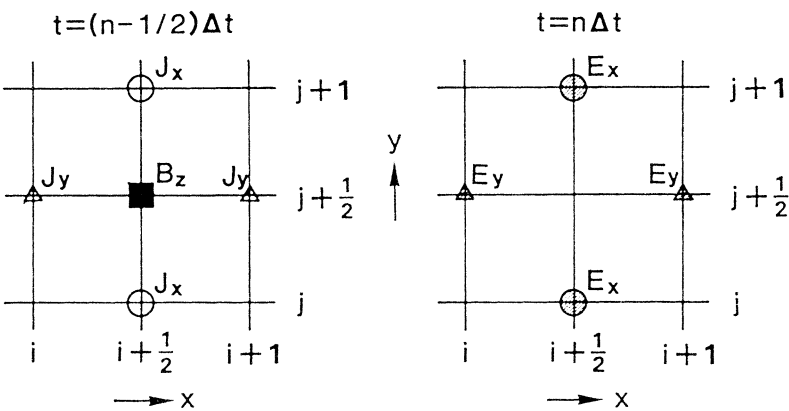
These equations (A) and (B) are solved as central difference equations in space and time by defining the E, B and J at the location shown in Figure 10-(a) and -(b) [Langdon and Lasinski, 1976]. For further reference we call the grid with label "i" a full grid (F) in x and the grid with label "i+1/2" a half grid (H) in x. Likewise, we call the grid with label "j" a full grid (F) in y and the grid with label "j+1/2" a half grid (H) in y. Combining x and y locations, we express the locations of the grid points with (i,j), (i+1/2,j), (i,j+1/2) and (i+1/2,j+1/2) by FF, HF, FH and HH.

The grid locations shown in Figure 10 are summarized as follows.

$E_x$	$B_x$	$J_x$	:	HF
$E_y$	$B_y$	$J_y$	:	FH
$E_z$	$B_z$	$J_z$	:	HH

The current densities  $J_x$ ,  $J_y$  and  $J_z$  are defined at different locations. To assign contributions of particles to the grid points, we have to calculate three different area-weightings. In order to reduce the CPU time in calculating area-weightings, we first calculate all  $J_x$ ,  $J_y$  and  $J_z$  at HH grid points, and then relocate  $J_x$  and  $J_y$  to HF

(A)



(B)

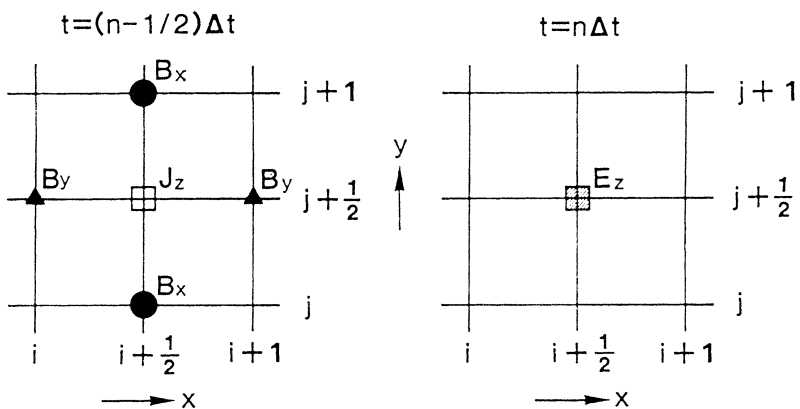


Figure 10. Allocation of field quantities to grid points: (a)  $E_x$ ,  $E_y$ ,  $B_z$ ,  $J_x$ ,  $J_y$  (b)  $E_z$ ,  $B_x$ ,  $B_y$ ,  $J_z$ .

and FH grid points by the following operations, respectively.

$$J_x^{'}_{i+1/2, j} = \frac{1}{2} ( J_x_{i+1/2, j-1/2} + J_x_{i+1/2, j+1/2} ) \quad (24)$$

$$J_y^{'}_{i, j+1/2} = \frac{1}{2} ( J_y_{i-1/2, j+1/2} + J_y_{i+1/2, j+1/2} ) \quad (25)$$

The relocation procedure has the effect of spatial filtering (see Section 3.4). This filtering reduces electromagnetic radiation loss at small wavelengths. As  $J_z$  is not relocated, it is necessary to apply the three point filtering to  $J_z$  both in x and in y directions. It is noted that filtering of  $J_x$  in x-direction and  $J_y$  in y-direction is not necessary at all. Because, fluctuations of  $J_x$  in x direction and  $J_y$  in y direction are not responsible to the electromagnetic radiations. In addition, The current density  $J$  and  $E$  must satisfy

$$\operatorname{div} ( J + \epsilon_0 \frac{\partial p}{\partial t} ) = 0 . \quad (26)$$

Since the electrostatic components  $E_x$  and  $E_y$  are calculated from the current distribution via Poisson's equation, the relocation of  $J_x$  in x and  $J_y$  in y only increases the inconsistency of  $J_x$  and  $J_y$  with  $E_x$  and  $E_y$ , respectively.

The electric fields  $E_x$  and  $E_y$  obtained by integrating Eqs. (19) and (20) are corrected by solving Poisson's equation using the charge density defined at FF grid points. If we calculate electric force acting on particles from the electric field  $E_x$  and  $E_y$  defined at HF and FH grid points, it results in a electrostatic self-force acting on particle, violating the momentum conservation as discussed in Section 2.1. The area weighting in calculation of the charge density and that in calculation of the force acting on particles must be identical and must be done using the quantities defined at the same grid locations. Since the charge density is defined at FF grid points, the electric field  $E_x$  and  $E_y$  obtained at FH and HF grid points must be relocated to the FF grid points before calculating the particle force. The above discussion of the electrostatic self-force is also applied to the magnetostatic force induce by Ampere's law  $\nabla \times B = \mu_0$ , which is rewritten as

$$\frac{\partial B_z}{\partial y} = \mu_0 J_x \quad (27)$$

$$- \frac{\partial B_z}{\partial x} = \mu_0 J_y \quad (28)$$

$$\frac{\partial B_y}{\partial x} - \frac{\partial B_x}{\partial y} = \mu_0 J_z \quad (29)$$

As the  $B_z$  is defined at HH grid points where  $J_x$  and  $J_y$  are also calculated by the area weighting scheme, The relations of Eqs. (28)

and (29) do not yield the self-force. However,  $B_x$  and  $B_y$  are defined at HF and FH grid points, while  $J_z$  is defined at HH grid points. In calculation of magnetic force acting on particles,  $B_x$  and  $B_y$  must be relocated to HH grid points.

Let us summarize the relocation procedure for elimination of the self-force.

$E_x$	:	HF	$\rightarrow$	FF
$E_y$	:	FH	$\rightarrow$	FF
$B_x$	:	HF	$\rightarrow$	HH
$B_y$	:	FH	$\rightarrow$	HH

$E_z$  and  $B_z$  are not relocated.

Owing to the relocation procedure, computing time for calculating the particle forces is reduced because the area weighting for FH and HF grid points are not computed any more. In calculation of electromagnetic forces acting on particles,  $E_x$  and  $E_y$  are interpolated from FF grid points and  $E_z$ ,  $B_x$ , while  $B_y$  and  $B_z$  are interpolated from HH grid points.

### 3.4 Digital Filtering

Spatial filterings of the quantities defined at grid points are generally used in order to eliminate nonphysical noises at short wavelengths, where the finite difference of the fields becomes most inaccurate. Two kinds of digital filtering schemes are used in the KEMPO. One is a filtering of two-point averaging as defined by

$$\phi_{i+1/2}' = \frac{1}{2} (\phi_i + \phi_{i+1}) \quad (30)$$

which is implicitly involved in the relocation procedure of the field quantities. The other is three-point digital filter or a binomial digital filter [Birdsall and Langdon, 1984] given as

$$\phi_i' = \frac{1}{4} (\phi_{i-1} + 2\phi_i + \phi_{i+1}) \quad (31)$$

which is explicitly used in the code. The attenuation factor of these two filters are given by the following equations.

Two-point digital filter :

$$\phi'(k) = \cos \frac{k\Delta x}{2} \phi(k) \quad (32)$$

Three-point digital filter :

$$\phi'(k) = \cos \left( \frac{k\Delta x}{2} \right)^2 \phi(k) \quad (33)$$

These filters are used in the following two manners. Firstly they are applied to the particle-pushing fields  $E_p$  and  $B_p$  in order to eliminate nonphysical random forces which causes stochastic heatings of particles. Since the relocation procedures implicitly involving the two-point filter are different for the components ( $E_x$ ,  $E_y$ , etc.) and for the directions (x and y), it is necessary to apply the three-point filter to the components and directions which are not affected by the relocation procedure. Secondly these filters are applied to the current density calculated from the particles. The current density is the source of electromagnetic radiations. Fluctuations at short wavelengths correspond to high frequency electromagnetic waves which undergo a damping by the time filtering of MTS scheme as time goes on. Due to the electromagnetic radiations which are to be damped by both spatial and time filtering, particles lose their thermal energy. In order to prevent the energy loss, it is necessary to eliminate fluctuations at short wavelength by the digital filters.

### 3.5 Unit System used in the KEMPO

It is noted that there is no necessity to stick to a real unit system like CGS or MKS unit system in simulations. What is important in simulations are ratios of quantities in the system, i.e., a ratio of a wave magnetic field to the static magnetic field, or a ratio of a kinetic energy to the total energy, etc.. In most of simulations physical quantities are normalized to the basic parameters in the system where the basic parameters are assumed to be unity. However, selections of basic parameters are different depending on physical models. In order to make the simulation code applicable to various problems of a wide range of parameters, we do not normalize any quantities, or rather we adopt a relative unit system where all parameters are calculated from a set of independent basic parameters via basic equations. These basic parameters are as follows.

1. Angular frequency (plasma, cyclotron, wave frequency etc.)  
 $\omega_{pi}$ ,  $\omega_{c1}$ ,  $\omega$
2. System length  $L_x$ ,  $L_y$
3. Charge-to-mass ratio  $(q/m)_i$
4. Number of superparticles in the system  $N_i$

where the subscript "i" denotes the i-th species of particles. Values of these four quantities are given arbitrary, except that ratios of quantities in the same units like  $\omega_{pi}/\omega_{c1}$ ,  $L_y/L_x$  or  $(q/m)_2/(q/m)_1$ , are kept the same as those of the real physical quantities. Especially, it is noted that numbers of superparticles have no relation to the real number densities in the plasma, and  $N_1$  and  $N_2$  are independent of each other.

The basic equations are written in the following form which is identical to those in MKS unit system.

## (1) Equations of motion

$$\frac{dr}{dt} = v \quad (34)$$

$$\frac{dv}{dt} = \frac{q_i}{m_i} (E + v \times B) \quad (35)$$

## (2) Maxwell's equations

$$\text{rot } B = \mu_0 J + \frac{1}{c^2} \frac{\partial E}{\partial t} \quad (36)$$

$$\text{rot } E = - \frac{\partial B}{\partial t} \quad (37)$$

$$\text{div } B = 0 \quad (38)$$

$$\text{div } E = \frac{\rho}{\epsilon_0} \quad (39)$$

where  $c$ ,  $\epsilon_0$  and  $\mu_0$  are the light speed, electric permittivity and magnetic permeability, respectively.

It is noted that  $\epsilon_0$  and  $\mu_0$  may be chosen arbitrary except that  $\epsilon_0 \mu_0 = 1/c^2$ . For simplicity, we define  $\epsilon_0 = 1$  and  $\mu_0 = 1/c^2$ , and the units of charge, mass, electric and magnetic fields are given based on their definition.

Other physical quantities are calculated via the following relations obtained from the basic equations. The cyclotron frequency of species 1 and the plasma frequencies of species i are given as

$$\omega_{c1} = \frac{q_1}{m_1} B_0, \quad \omega_{pi} = \left( \frac{n_i q_i^2}{m_i \epsilon_0} \right)^{\frac{1}{2}} \quad (40)$$

where  $n_i$  is a particle density of species i defined as a density in the two dimensional system of  $L_x \times L_y$ .

## -Particle density

$$n_i = \frac{N_i}{L_x L_y} \quad (41)$$

From (40) and (41) we can calculate the following physical quantities.

## -Charge of a particle

$$q_i = \frac{\epsilon_0 L_x L_y \omega_{pi}^2}{N_i (q/m)_i} \quad (42)$$

-Mass of a particle

$$m_i = \frac{\epsilon_0 L_x L_y \omega_{pi}^2}{N_i (q/m)_i^2} \quad (43)$$

-Static magnetic field

$$B_0 = \frac{\omega_{c1}}{(q/m)_i} \quad (44)$$

It is noted that the mass  $m_i$  and charge  $q_i$  have little physical meaning in the relative unit system. What are physically meaningful are the mass density  $m_i n_i$  and charge density  $q_i n_i$  given as

$$q_i n_i = \frac{\epsilon_0 \omega_{pi}^2}{(q/m)_i}, \quad m_i n_i = \frac{\epsilon_0 \omega_{pi}^2}{(q/m)_i^2} \quad (45)$$

The values of  $\omega_{pi}$  and  $(q/m)_i$  of different species must be given based on the ratios in the physical model.

### 3.6 Rescaling of Physical Quantities

In order to attain computational efficiency, it is necessary to reduce the number of operations involved in difference equations of fields and particles. Since operations of multiplying and dividing by  $\Delta r$ ,  $\Delta t/2$  and  $(q/m)$  are frequently used in the difference equations, we rescale the distance, time and charge-to-mass-ratio expressed in the relative unit by  $\Delta r$ ,  $\Delta t/2$  and  $(q/m)_i$ , respectively. Other physical quantities are rescaled as follows.

distance	$r^* = (1/\Delta r) r$
time	$t^* = (2/\Delta t) t$
velocity	$v^* = (\Delta t/2)(1/\Delta r) v$
number density	$n^* = (\Delta r)^2 n$
charge	$q^* = (q/m)_i (\Delta t/2)^2 (1/\Delta r)^2 q$
mass	$m^* = (q/m)_i^2 (\Delta t/2)^2 (1/\Delta r)^2 m$
Electric field	$E^* = (q/m)_i (\Delta t/2)^2 (1/\Delta r) E$
Magnetic field	$B^* = (q/m)_i (\Delta t/2) B$
Current density	$J^* = (q/m)_i (\Delta t/2)^3 (1/\Delta r) J$
Electric potential	$\phi^* = (q/m)_i (\Delta t/2)^2 (1/\Delta r)^2 \phi$
Charge density	$\rho^* = (q/m)_i (\Delta t/2)^2 \rho$
Energy density	$\sigma^* = (q/m)_i^2 (\Delta t/2)^4 (1/\Delta r)^2 \sigma$

quantities with \* are rescaled ones.

The difference equations of particle motion of species 1 are written as in the following simple forms. The \*'s on  $r$ ,  $t$ ,  $v$ ,  $n$ ,  $q$ ,  $m$ ,  $E$ ,  $B$ ,  $J$ ,  $\phi$ ,  $\rho$  and  $\sigma$  are omitted hereafter.

$$\mathbf{v}^- = \mathbf{v}^{n-1/2} + \mathbf{E}^n \quad (46)$$

$$\mathbf{v}' = \mathbf{v}^- + \mathbf{v}^- \times \mathbf{B}^n \quad (47)$$

$$\mathbf{v}^+ = \mathbf{v}^- + \frac{2}{1 + (\mathbf{B}^n)^2} \mathbf{v}' \times \mathbf{B}^n \quad (48)$$

$$\mathbf{v}^{n+1/2} = \mathbf{v}^+ + \mathbf{E}^n \quad (49)$$

$$\mathbf{r}^{n+1/2} = \mathbf{r}^n + \mathbf{v}^{n+1/2} \quad (50)$$

$$\mathbf{r}^{n+1} = \mathbf{r}^{n+1/2} + \mathbf{v}^{n+1/2} \quad (51)$$

For the  $i$ -th species of particles ( $i \neq 1$ ),  $E$  and  $B$  must be multiplied by  $(q/m)_i / (q/m)_1$ .

The difference equations for fields are written as

$$\mathbf{B}^n = \mathbf{B}^{n-1/2} - \nabla^* \times \mathbf{E}^n \quad (52)$$

$$\mathbf{B}^{n+1/2} = \mathbf{B}^n - \nabla^* \times \mathbf{E}^n \quad (53)$$

$$\mathbf{E}^{n+1} = \mathbf{E}^n + 2c^2 \nabla^* \times \mathbf{B}^{n+1/2} + 2\mathbf{J}^{n+1/2} \quad (54)$$

where the operation  $\nabla^* \times A_{i,j}$  ( $A = E$  or  $B$ ) are realized by the following simple operations.

$$(\nabla^* \times A_{i,j})_x = A_{z,i,j+1} - A_{z,i,j} \quad (55)$$

$$(\nabla^* \times A_{i,j})_y = A_{z,i,j} - A_{z,i+1,j} \quad (56)$$

$$(\nabla^* \times A_{i,j})_z = A_{y,i+1,j} - A_{y,i,j} - A_{x,i,j+1} + A_{x,i,j} \quad (57)$$

The rescaling is performed after all the input parameters are given to the simulation code, and all the output data are reconverted again to the values in the relative unit system. Since all input and output data are expressed in the relative unit system, users of the code do not have to be familiar with the rescaling inside the code.

#### 4. LONG TIME SCALE CODE FOR MONOCHROMATIC WHISTLER INTERACTION

Simplification and reduction of CPU time is attainable in particle simulations by limiting the allowed wave modes in the simulation to a monochromatic wave with the assumption of slow

variations in amplitude and frequency. This code is called the Long-Time-Scale (LTS) code [Rathmann et al., 1978, Omura and Matsumoto, 1981]. Instead of solving the Maxwell equations and equations of motion of all particles as is usually done in the conventional electromagnetic codes, only the wave amplitude, frequency and wavenumber of a monochromatic wave is incremented forwards in time with a self-consistent updating of charge and current density calculated from numerical solutions to the equation of motion obtained solely for resonant particles in the monochromatic wave.

Basic equations for the monochromatic whistler mode wave and resonant electrons are described in Sections 4.1 and 4.2, respectively [Omura and Matsumoto, 1981]. These equations are coded into difference equations in Sections 4.3 and 4.4. The flow chart of LTS whistler simulation is given in Sections 4.5.

#### 4.1 Equations for the Wave Fields

We assume a purely transverse whistler mode wave which propagates along the geomagnetic field line and interacts with counter-streaming high energy resonant electrons existing in the magnetosphere. We use a right-handed coordinate system;  $z$  being a distance along the field line from the equatorial plane, and  $x$  and  $y$  axes being perpendicular to the external magnetic field. For convenience the wave fields are expressed in complex variables with dot marks on their top. The  $x$  and  $y$  components are represented by real and imaginary parts of the complex quantities, respectively.

$$\dot{B}_W = B_{WX} + iB_{WY}, \quad \dot{E}_W = E_{WX} + iE_{WY} \quad (58)$$

Neglecting the term for the displacement current in Maxwell's equation, and dividing a conduction current into a cold plasma current  $j_C$  and an energetic resonant electron current  $j_R$ , we have Maxwell's equations in the form

$$i \frac{\partial E_W}{\partial z} = - \frac{\partial B_W}{\partial t}, \quad i \frac{\partial B_W}{\partial z} = \mu_0 (j_C + j_R). \quad (59)$$

The linearized momentum equation of the cold electrons is

$$\frac{\partial \dot{j}_e}{\partial t} - i\Omega_e \dot{j}_C = \epsilon_0 \Pi_e^2 \dot{E}_W \quad (60)$$

where  $\Omega_e$  and  $\Pi_e$  are the electron cyclotron and plasma frequencies, respectively. Eliminating  $j_C$  and  $E_W$  from (59) and (60), we have

$$\left[ \frac{\partial}{\partial z} \left( \frac{\partial}{\partial t} - i\Omega_e \right) \frac{\partial}{\partial z} - \frac{\Pi_e^2}{c^2} \frac{\partial}{\partial t} \right] \dot{B}_W = -i \mu_0 \left( \frac{\partial}{\partial t} - i\Omega_e \right) \frac{\partial}{\partial z} j_R \quad (61)$$

where we have assumed that the inhomogeneity of the medium is sufficiently small within a distance of the wave length, i.e.,

$$\left| \frac{\partial \Omega_e}{\partial z} \right| \ll |k(\omega - \Omega_e)| , \quad \left| \frac{\partial \Pi_e^2}{\partial z} \right| \ll |k\Pi_e^2| . \quad (62)$$

The quantities  $\dot{B}_w$  and  $\dot{J}_R$  are expressed in terms of the amplitude  $B_w$ ,  $J_R$  and phase  $\psi$  and  $\psi + \Psi_R$  as

$$\dot{B}_w = B_w \exp \{i\psi\} , \quad \dot{J}_R = J_R \exp \{i(\psi + \Psi_R)\} \quad (63)$$

where  $\Psi_R$  is a relative phase angle between  $J_R$  and  $B_w$ , and is assumed to be a slowly varying function with respect to time and space.

The frequency  $\omega$  and wavenumber  $k$  for the right-handed polarized wave are defined by

$$\omega = \frac{\partial \psi}{\partial t} , \quad k = - \frac{\partial \psi}{\partial z} . \quad (64)$$

We assume here that the terms involving the first-order time and space derivatives of  $k$ ,  $J_R$  and  $\Psi_R$  as well as the second-order derivatives of  $B_w$  are negligible. Substitution of (63) into (61) yields

$$\begin{aligned} & \left( k^2 + \frac{\Pi_e^2}{c^2} \right) \frac{\partial B_w}{\partial t} + 2k(\Omega_e - \omega) \frac{\partial B_w}{\partial z} - i \left\{ k^2(\Omega_e - \omega) - \frac{\Pi_e^2}{c^2} \omega \right\} B_w \\ &= \mu_0 k (\Omega_e - \omega) (J_R \sin \Psi_R - i J_R \cos \Psi_R) \end{aligned} \quad (65)$$

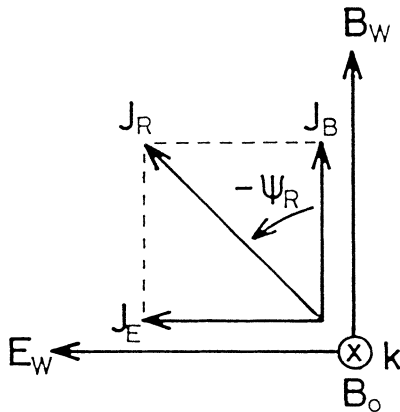


Figure 11. Configuration of the wave magnetic ( $B_w$ ) and electric ( $E_w$ ) fields, wavenumber vector ( $k$ ), external magnetic field ( $B_w$ ), and resonant current ( $J_R$ ) and its components  $J_B$  and  $J_E$ .

Separating imaginary and real parts in (65), we have

$$(k^2 + \frac{\Pi_e^2}{c^2}) \frac{\partial B_w}{\partial t} + 2k(\Omega_e - \omega) \frac{\partial B_w}{\partial z} = -\mu_0 k(\Omega_e - \omega) J_E \quad (66)$$

$$\{k^2(\Omega_e - \omega) - \frac{\Pi_e^2}{c^2}\omega\} B_w = \mu_0 k(\Omega_e - \omega) J_B \quad (67)$$

where

$$J_E = J_R \sin(-\psi_R) , \quad J_B = J_R \cos(-\psi_R) , \quad (68)$$

and  $J_E$  and  $J_B$  are the components of the transverse resonant current  $J_R$  parallel to the wave electric field  $E_w$ , and to the wave magnetic field  $B_w$ , respectively (see Figure 11). These  $J_E$  and  $J_B$  are calculated by the following equations

$$J_E = -e \sum_i v_{\perp i} \sin(-\xi_i) \quad J_B = -e \sum_i v_{\perp i} \cos(-\xi_i) \quad (69)$$

where  $v_{\perp i}$  is a velocity component perpendicular to the external magnetic field and  $\xi_i$  is a phase angle between  $v_{\perp i}$  and  $B_w$ , and  $\Sigma$  is taken over resonant electrons in a unit cell. Since the group velocity is expressed by

$$v_g = \frac{2k(\Omega_e - \omega)}{k^2 + (\Pi_e^2/c^2)} \quad (70)$$

we have from (66)

$$\frac{\partial B_w}{\partial t} = -v_g \left( \frac{\partial B_w}{\partial z} + \frac{1}{2} \mu_0 J_E \right) \quad (71)$$

The second order differentiation of the wave phase  $\psi$  gives a relation of  $k$  and  $\omega$  as

$$\frac{\partial k}{\partial t} = -\frac{\partial \omega}{\partial z} \quad (72)$$

Using (71) and (72), we can follow the time evolution of  $B_w$  and  $k$ , while the frequency  $\omega$  is calculable from (67) which is rewritten as

$$\omega = \frac{k(k - \mu_0 J_B / B_w)}{k(k - \mu_0 J_B / B_w) + \Pi_e^2 / c^2} \Omega_e \quad (73)$$

As is seen in (71) and (73),  $J_E$  causes a change of the wave amplitude  $B_w$ , and  $J_B$  modifies the frequency  $\omega$ .

#### 4.2 Equations of Motion of Resonant Electrons

We have derived the wave equations showing how the wave is modified by the presence the resonant current  $J_R$ , which is formed as a result of cyclotron resonance between hot electrons and the wave. The equations of motion of resonant electrons are expressed in the

following form. We introduce polar coordinates ( $v_{\parallel}$ ,  $v_{\perp}$ ,  $\phi$ ) for the velocity, where  $v_{\parallel}$  and  $v_{\perp}$  are the velocity components parallel and perpendicular to the external geomagnetic field respectively, and  $\phi$  is the Larmor phase angle of  $v_{\perp}$  in the rest frame. Equations of motion are then expressed as [e.g. Dysthe, 1971]

$$\frac{dv_{\parallel}}{dt} = \Omega_w v_{\perp} \sin(\phi - \psi) - \frac{v_{\perp}^2}{2\Omega_e} \frac{\partial \Omega_e}{\partial z} \quad (74)$$

$$\frac{dv_{\perp}}{dt} = \Omega_w \left( \frac{\omega}{k} - v_{\parallel} \right) \sin(\phi - \psi) + \frac{v_{\parallel} v_{\perp}}{2\Omega_e} \frac{\partial \Omega_e}{\partial z} \quad (75)$$

$$\frac{d\phi}{dt} = \frac{\Omega_w}{v_{\perp}} \left( \frac{\omega}{k} - v_{\parallel} \right) \cos(\phi - \psi) + \Omega_e \quad (76)$$

$$\frac{dz}{dt} = v_{\parallel} \quad (77)$$

where the wave amplitude  $B_w$  is replaced by  $\Omega_w = eB_w/m$ . The first terms in the right-hand sides of (74) ~ (76) correspond to the effect of the wave, while the second terms express the effect of the external geomagnetic field. The effect of the inhomogeneity of the medium is expressed by the second terms in (74) and (75), which disappear in a homogeneous case, as well as by  $k$  and  $\Omega_e$  in (74) ~ (76), which vary slowly with the distance in the present model.

#### 4.3 Particle Pushing Algorithm

The equations for the wave field (71) and (73) shows that the resonant currents  $J_E$  and  $J_B$  control the evolution of the monochromatic whistler wave. The resonant currents are calculated by solving the equations (74) ~ (77) of motion for a large number of hot electrons. An algorithm used in a "long-time-scale (LTS)" code for a whistler simulation first proposed by Rathmann et al. [1978] is adopted for particle pushing in the present simulation. The increments of the quantities  $v_{\parallel}$ ,  $v_{\perp}$ ,  $\phi$  and  $z$  over a time step  $\delta t$  are separated into increments due to the wave and increments due to the cyclotron motion in the external magnetic field. The particle pushing algorithm takes the form of

$$f(t_{n+1}) = f(t_n) + \delta f_w + \delta f_c , \quad (78)$$

where  $t_{n+1} = t_n + \delta t$ , and  $f$  is a quantity such as  $v_{\parallel}$ ,  $v_{\perp}$ ,  $\phi$  and  $z$ .  $\delta f_w$  and  $\delta f_c$  are increments due to the wave and due to the cyclotron motion, respectively, and they are obtained by integrating (74) ~ (77) over the time interval from  $t_n$  to  $t_{n+1}$  under the conditions that  $|\delta v_{\parallel}| \ll |v_{\parallel}|$ ,  $|\delta v_{\perp}| \ll v_{\perp}$ ,  $|\delta k| \ll k$ ,  $|\delta \Omega_e| \ll |\Omega_e|$ ,  $|\delta \omega| \ll \omega$ , and  $|\delta \Omega_w| \ll \Omega_w$ . The increments due to the wave are expressed in terms of the quantities at  $t = t_n$  as

$$\delta v_{\parallel w} = \frac{\Omega_w v_{\perp}}{\zeta} \delta \cos \zeta \quad (79)$$

$$\delta v_{\perp w} = - \frac{\Omega_w}{\zeta} \left( \frac{\omega}{k} - v_{\parallel} \right) \delta \cos \zeta \quad (80)$$

$$\delta \phi_w = \frac{\Omega_w}{v_{\perp} \zeta} \left( \frac{\omega}{k} - v_{\parallel} \right) \delta \sin \zeta \quad (81)$$

$$\delta z_w = \frac{\Omega_w v_{\perp}}{\zeta^2} (\zeta' \delta t \cos \zeta - \delta \sin \zeta) \quad (82)$$

where

$$\delta \cos \zeta = \cos(\zeta + \zeta' \delta t) - \cos \zeta, \quad \delta \sin \zeta = \sin(\zeta + \zeta' \delta t) - \sin \zeta \quad (83)$$

and  $\zeta$  is a relative phase angle between  $v_{\perp}$  and  $B_w$ , i.e.,  $\phi - \psi$ .  $\zeta'$  denotes a time derivative of  $\zeta$  obtained from (76), i.e.,

$$\zeta' = \frac{\Omega_w}{v_{\perp}} \left( \frac{\omega}{k} - v_{\parallel} \right) \cos \zeta + \Omega_e - \omega + kv_{\parallel} \quad (84)$$

When  $\zeta' \cong 0$ , (79) ~ (82) are not appropriate because the right hand sides of these equations shows an overflow in the calculation process. In this case the first terms of (74), (75) and (76) are directly integrated assuming  $\zeta$  is almost constant, and we have

$$\delta v_{\parallel w} = \delta t \Omega_w \sin \zeta \quad (85)$$

$$\delta v_{\perp w} = \delta t \Omega_w \left( \frac{\omega}{k} - v_{\parallel} \right) \sin \zeta \quad (86)$$

$$\delta \phi_w = \frac{\delta t \Omega_w}{v_{\perp}} \left( \frac{\omega}{k} - v_{\parallel} \right) \cos \zeta \quad (87)$$

$$\delta z_w = - \frac{1}{2} \delta v_{\parallel w} \delta t \quad (88)$$

The increments due to the cyclotron motion are expressed as

$$\delta v_{\parallel c} = - \frac{v_{\perp}^2}{2v_{\parallel}} \frac{\Omega_e(z + v_{\parallel} \delta t) - \Omega_e(z)}{\Omega_e(z)} \quad (89)$$

$$\delta v_{\perp c} = \frac{v_{\perp}}{2} \frac{\Omega_e(z + v_{\parallel} \delta t) - \Omega_e(z)}{\Omega_e(z)} \quad (90)$$

$$\delta\phi_C = \frac{\delta t}{2} \{ \Omega_e(z) + \Omega_e(z + v_{||}\delta t) \} \quad (91)$$

$$\delta z_C = \delta t \{ v_{||} + \frac{\delta v_{||C}}{2} \} \quad (92)$$

In the simulation,  $w$ ,  $\omega$ ,  $k$  and  $\phi$  are calculated at the spatial grid points, and to obtain these quantities at particle position  $z$ , we interpolated from values of the neighboring grid points  $Z_m$  and  $Z_{m+1}$  in the manner as

$$F(z) = F(Z_m) + \frac{F(Z_{m+1}) - F(Z_m)}{\Delta Z} (z - Z_m) \quad (93)$$

where  $F$  corresponds to quantities such as  $w$ ,  $\omega$  or  $k$ , and  $\Delta Z$  is the grid spacing defined by  $\Delta Z = Z_{m+1} - Z_m$ . Integration of  $k(z)$  expressed by (93) gives the phase of the wave,

$$\Psi(z) = \Psi(Z_m) - k(Z_m)(z - Z_m) - \frac{k(Z_{m+1}) - k(Z_m)}{2\Delta Z} (z - Z_m)^2 \quad (94)$$

In the simulations presented in Section 6, we take into account the inhomogeneity of the geomagnetic field which is approximated by a dipole magnetic field given by the following equations.

$$B_0 = B_{0S} \left( \frac{R_E}{R} \right)^3 \sqrt{1 + 3 \sin^2 \Phi} \quad (95)$$

$$R = R_E L \cos^2 \Phi \quad (96)$$

$$\frac{z}{R} = \frac{1}{2\sqrt{3}} (x + \sinh x \cosh x) \quad (97)$$

$$x = \sqrt{3} \sin \Phi \quad (98)$$

where  $\Phi$  and  $R$  are a geomagnetic latitude and a distance to the concerned point from earth's center. The quantities  $B_0$  and  $B_{0S}$  are magnetic fields at  $(R, \Phi)$  and at the earth's surface, respectively.  $R_E$  and  $L$  are the radius of the earth (6370km) and geocentric distance at the equatorial plane normalized to  $R_E$ . The quantity  $z$  is a distance measured along the geomagnetic field line from the equatorial plane to the concerned point. Let  $B_{0EQ}$  denote the magnetic field at  $R = LR_E$  in the equatorial plane, then we have from (95)

$$B_{0EQ} = L^{-3} B_{0S} \quad (99)$$

Substituting (96), (97) and (98) into (95), we express  $B_0$  in term of  $B_{0EQ}$  and  $z$  as,

$$B_0 = B_{0EQ} \frac{\sqrt{1 + x^2}}{(1 - x^2/3)^3} \quad (100)$$

where  $x$  is given as a solution of the following equation.

$$F(x, z) = x + \sinh x \cosh x - \frac{2\sqrt{3} z}{LR_E} = 0 \quad (101)$$

From (100) and (81) we can calculate an external magnetic field at each grid point.

#### 4.4 Field Updating Algorithm

In the previous section the algorithm for updating physical quantities associated with each particle was discussed. This section presents the method to update the quantities which are assigned to the spatial grid points. These quantities are the wave amplitude  $B_w$  and its time derivative  $\partial B_w / \partial t$ , the wavenumber  $k$  and its time derivative  $\partial k / \partial t$ , the wave frequency  $\omega$  and the wave phase  $\psi$  in the rest frame, and the resonant current  $J_E$  and  $J_B$ .

The wave amplitude and the wavenumber are advanced over the time step  $\delta t$  using their time derivatives at  $t = t_n$ , i.e.,

$$B_{wm}(t_{n+1}) = B_{wm}(t_n) + \left(\frac{\partial B_w}{\partial t}\right)_m(t_n) \delta t \quad (102)$$

$$k_m(t_{n+1}) = k(t_n) + \left(\frac{\partial k}{\partial t}\right)_m(t_n) \delta t \quad (103)$$

where the subscript  $m$  denotes a value at a grid point  $Z_m$ . The wave phase is first advanced at the boundary grid  $Z_1$  and extended successively to the next grid by integrating  $k$  over the grid spacing as

$$\psi_1(t_{n+1}) = \psi_1(t_n) + \omega(t_n) \delta t \quad (104)$$

$$\psi_{m+1}(t_{n+1}) = \psi_m(t_{n+1}) - \frac{1}{2} (k_m(t_{n+1}) + k_{m+1}(t_{n+1})) \Delta Z \quad (105)$$

After the quantities  $z_i$ ,  $v_{\perp i}$ ,  $v_{\parallel i}$  and  $\phi_i$  of each resonant particle and the wave phase  $\psi$  are updated, the resonant current  $J_E$  and  $J_B$  can be calculated. An electron in the particle simulation is not a "real electron", but it is a superparticle which represents a number of electrons in the real plasma. Therefore, we assign a density  $n_s$  to each superparticle (we may regard it a super-electron with a charge  $-n_s e$ ), and each super-particle forms resonant currents  $j_{Ei}$  and  $j_{Bi}$

$$j_{Ei} = -n_s e \sin(-\xi_i) , \quad j_{Bi} = -n_s e \cos(-\xi_i) \quad (106)$$

where  $i$  denotes a quantity of each particle; and  $\xi_i = \phi_i - \psi(z_i)$  and  $\psi(z_i)$  is calculated by (94). These  $j_{Ei}$  and  $j_{Bi}$  are assigned to the

neighboring grid points  $Z_m$  and  $Z_{m+1}$  ( $Z_m < z_i < Z_{m+1}$ ) with the first order particle weighting, or particle-in-cell (PIC) model [e.g. Birdsall and Langdon, 1984]. Resonant currents assigned to grid  $Z_m$  and  $Z_{m+1}$  are thus obtained by

$$J_{Em,i} = j_{Ei} \frac{Z_{m+1} - z_i}{\Delta Z}, \quad J_{E(m+1),i} = j_{Ei} \frac{z_i - Z_m}{\Delta Z} \quad (107)$$

and  $J_{Bm,i}$  and  $J_{B(m+1),i}$  are given in the same manner as above. Summing the currents  $J_{Em,i}$  and  $J_{Bm,i}$  over all particles between  $Z_{m-1}$  and  $Z_{m+1}$  gives the resonant currents  $J_{Em}$  and  $J_{Bm}$  at a grid point  $Z_m$ .

When the resonant currents are obtained, the wave frequency  $\omega$  and the time derivatives  $\partial B_w / \partial t$  and  $\partial k / \partial t$  are calculated through (71), (72) and (73) as follows.

$$\omega_m = \frac{k_m (\omega_m - \mu_0 J_{Bm} / B_{wm})}{k_m (\omega_m - \mu_0 J_{Bm} / B_{wm}) + \Pi_{Em}^2 / c^2} \quad (108)$$

$$(\frac{\partial B_w}{\partial t})_m = - \frac{2k_m (\Omega_{Em} - \omega_m)}{k^2 + \Pi_{Em}^2 / c^2} \left( \frac{B_{wm} - B_{w(m-1)}}{\Delta Z} + \frac{1}{2} \mu_0 J_{Em} \right) \quad (109)$$

$$(\frac{\partial k}{\partial t})_m = - \frac{\omega_{m+1} - \omega_{m-1}}{2\Delta Z} \quad (110)$$

As (109) and (110) contain the terms of spatial finite differentiation, the boundary conditions must be chosen carefully. In the present simulation we assume the wave propagating from the left boundary  $Z_1$  to the right boundary  $Z_M$ . The wave field at  $Z_M$  is reasonably extrapolated from the field at  $Z_{M-1}$  and  $Z_{M-2}$  as

$$B_{wM} = 2B_{w(M-1)} - B_{w(M-2)} \quad (111)$$

and  $\omega_M$  and  $k_M$  are also extrapolated in the same manner. At the left boundary  $Z_1$ , however, extrapolation from  $Z_2$  and  $Z_3$  is not applicable, because the wave propagates from  $Z_1$  to  $Z_2$  and  $Z_3$ . In the simulation where the wave is externally injected from the boundary, the wave field at  $Z_1$  is given arbitrarily. In the simulation where a self-evolution of a uniform and periodic wave-particle interaction is followed, the field at  $Z_1$  is set equal to the field at  $Z_2$ .

$J_{Bm}/B_{wm}$  in (108) causes a non-physical fluctuation of  $\omega$ , when the wave amplitude  $B_w$  becomes very small, because the resonant current  $J_{Bm}$  calculated from a limited number of particles necessarily contains some numerical fluctuations. This difficulty is relieved by assuming a thermal magnetic noise level  $B_{th}$  in the magnetospheric plasma, and setting the term  $J_{Bm}/B_{wm}$  equal to  $J_{Bm}/B_{th}$  when  $B_{wm} < B_{th}$ . In the simulation presented in Section 6.3 we follow evolution of a wave whose amplitude is  $B_w = 10^{-5} \sim 10^{-6} B_0$ , and  $B_{th}$  is chosen as  $B_{th} = 10^{-6} B_0$ .

#### 4.5 Flow Chart of Long Time Scale Whistler Simulation

Recurrent use of the particle pushing and field updating algorithms enables us to follow a self-consistent evolution of the whistler wave-particle interaction. Motion of cold plasma particles which support the wave propagation is not solved, because its effect is implicitly included in the wave equation (71) and (73). Computing time is greatly saved by not solving equations of motion for cold electrons. It is noted that there is no necessity to choose the time step as  $\delta t \cdot \text{Max}(\Omega_e, \Pi_e) \ll 1$  which is usually a necessary condition in the usual particle simulation of plasmas. One requirement of the time step is  $\delta t \cdot \omega_t \ll 1$ , where  $\omega_t$  is the trapping frequency given by  $\omega_t = (kv_1\Omega_w)^{1/2}$ . The relative phase angles  $\zeta$ 's of the resonant particles trapped in the wave potential change their phase angle  $\zeta$ 's with a time scale of  $\omega_t^{-1}$  and thus the resonant currents controlling the wave evolution vary with  $\omega_t$ . Another requirement is that  $V_{\max} \delta t \leq \Delta Z$ , where  $V_{\max}$  is the maximum velocity both in the wave group velocity and in the velocities of particles in the system. This is the loosest condition that must be satisfied in the difference scheme used in the algorithm.

The present simulation method is basically the long-time-scale (LTS) algorithm first formulated by Rathmann et al. [1978]. In their algorithm, however, they follow the time evolution of the wave frequency  $\omega$  using the equation

$$\frac{\partial \omega}{\partial t} + V_g \frac{\partial \omega}{\partial z} = - \frac{\mu_0}{2k} V_g \frac{\partial}{\partial t} \left( \frac{k J_B}{B_w} \right) \quad (112)$$

which is obtained by differentiating (67) with time  $t$  under the assumption that the cold plasma dispersion relation without the contribution of hot resonant electrons is valid. We found this equation vulnerable to a numerical instability because of the time differentiation of  $k J_B / B_w$  which picks up numerical fluctuations of  $J_B$ , where  $J_B$  is calculated from a limited number of particles and correspondingly involves statistical errors. Actually, (112) is not necessary in the algorithm if the phase relation (72) is made use of to follow the time evolution of the wavenumber  $k$ . In our method the frequency  $\omega$  is determined by (73) as a function of  $k$  and  $J_B / B_w$  after advancing  $k$  in time by (72). In the method of Rathmann et al., however, the wavenumber  $k$  is determined by (67) or (73) as a function of  $\omega$  and  $J_B / B_w$  after advancing in time by (112). The flow chart of the LTS simulation is shown in Figure 12.

### FLOW CHART OF LTS WHISTLER SIMULATION

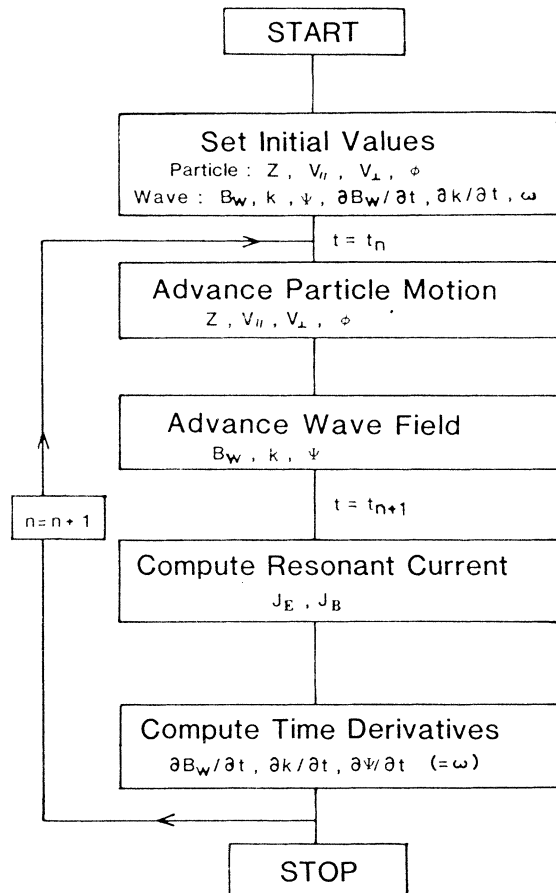


Figure 12. Flow chart of LTS whistler simulation.

## 5. DIAGNOSTIC TOOLS

### 5.1 Diagnostic Routines and Post-processors

We understand physical processes in a simulation run only through various diagnoses of the simulation data. Good and systematic diagnoses are needed for quick and good understanding of the simulated process. Diagnostic processes of a simulation consist of two steps. One is to use a diagnostic routine in a simulation code (main program), and the other is to use a group of diagnostic programs called post-processors.

The diagnostic routine stores simulation data into data files at a specified time interval. Data to be stored are specified depending on physical problems to be simulated, such as one of three components of the electric fields at grid points or part of particle velocities and positions. It is not realistic to store all the physical quantities at every time step due to a limitation of available data storage systems. The diagnostic routine also calculate wave and particle energies and distribution functions of particles simultaneously in a simulation run, and print them out or store them into data files. These in-run diagnoses become very important in a large scale of simulations, because they can extract necessary information from a large amount of physical quantities all of which are unable to be stored to files at each time step.

Post-processors give analyses of simulation data stored by the diagnostic routine in a simulation code and produce various graphic outputs such as a time history of wave and particle energies or phase space plots of particles at a certain time. Some typical post-processors of KEMPO and KULTS codes are introduced with their graphic outputs in the following sections. Well organized graphic libraries and sophisticated graphic systems are necessary for development and efficient use of post-processors.

### 5.2 Energy History

If a simulation code assumes a periodic boundary condition, total energy which is a summation of wave and particle energies must be conserved. Therefore, the energy diagnosis is a very basic and important step in checking a validity of the simulation code. We can also extract information from the data about physical process of energy transfer between wave and particles or among different particle species.

In the KEMPO we calculate average energy densities of electric, magnetic and kinetic energies in a simulation system.

## (1) Electric energy density

$$\begin{aligned} w_E &= w_{Ex} + w_{Ey} + w_{EZ} \\ &= \frac{\epsilon_0}{2} \frac{1}{N_x N_y} \sum_{i=1}^{N_x} \sum_{j=1}^{N_y} (E_{xi,j}^2 + E_{yi,j}^2 + E_{zi,j}^2) \end{aligned} \quad (113)$$

## (2) Magnetic energy density

$$\begin{aligned} w_B &= \frac{1}{2\mu_0} \frac{1}{N_x N_y} \sum_{i=1}^{N_x} \sum_{j=1}^{N_y} \\ &\cdot \{(B_{xi,j} - B_{ox})^2 + (B_{yi,j} - B_{oy})^2 + (B_{zi,j} - B_{oz})^2\} \end{aligned} \quad (114)$$

It is noted that we do not include the static magnetic energy density in the magnetic energy density.

## (3) Kinetic energy density

$$\begin{aligned} K_S &= K_{Sx} + K_{Sy} + K_{Sz} \\ &= \frac{m_S}{2L_x L_y} \sum_{i=1}^{N_s} (v_{xi}^2 + v_{yi}^2 + v_{zi}^2), \end{aligned} \quad (115)$$

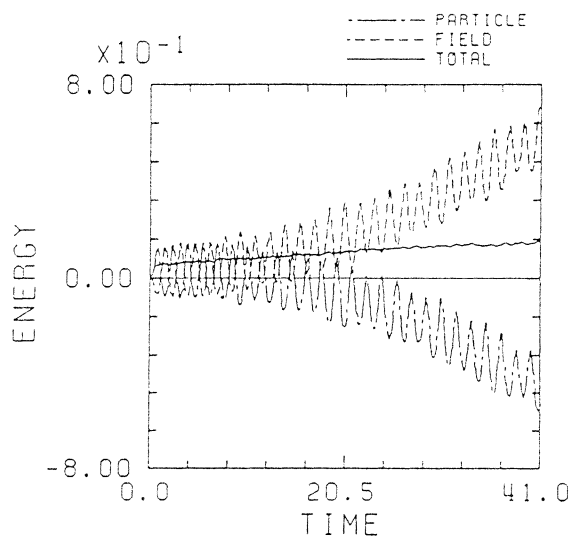


Figure 13. Time history of variations of total, field and particle energy densities.

where subscript "s" denotes quantities of particle species  $s$ . The total energy density ( $W_E + W_B + \Sigma K_S$ ) must be conserved in a periodic model.

The kinetic energy density  $K_S$  is divided into two components, i.e., a drift energy density  $K_{Sd}$  and a thermal energy density  $K_{St}$  calculated by

$$\begin{aligned} K_{Sd} &= K_{Sdx} + K_{Sdy} + K_{Sdz} \\ &= \frac{m_s}{2L_x L_y} \left\{ \left( \sum_{i=1}^N v_{xi} \right)^2 + \left( \sum_{i=1}^N v_{yi} \right)^2 + \left( \sum_{i=1}^N v_{zi} \right)^2 \right\} \quad (116) \end{aligned}$$

$$\begin{aligned} K_{St} &= K_{Stx} + K_{sty} + K_{stz} \\ &= (K_{sx} - K_{Sdx}) + (K_{sy} - K_{Sdy}) + (K_{sz} - K_{Sdz}) \end{aligned}$$

In the diagnostic routine in the KEMPO, all three components of  $W_E$ ,  $W_B$ ,  $K_S$  and  $K_d$  are calculated and stored into files at specified time intervals. The post processor combines these data and plots a time history of various energy densities. An example of history plots of energy variations is given in Figure 13.

### 5.3 $\omega$ - k Diagram

Fourier analysis of wave field data in space and time yields wave spectra in frequency  $\omega$  and wavenumber  $k$ . For simplicity, we limit spatial variations to one dimension, i.e., the x-direction in the following explanation. The wave field data are one of three components of electric or magnetic fields, which are stored into files by the diagnostic routine with a format as

$$[a(x_i, t_j)] \quad (i = 1, 2, \dots, N_x; j = 1, 2, \dots, M) \quad (118)$$

where  $N_x$  is a number of grid points in a system and  $M$  is a number of data in time sequence.

We assume a presence of a wave mode with frequency  $\omega$  and wavenumber  $k$  in the field data as

$$A_1 \sin(\omega t - kx + \theta_1) + A_2 \sin(\omega t + kx + \theta_2) \quad (119)$$

which is a summation of a forward traveling wave and backward traveling wave. Fourier analysis of  $[a(x_i, t_j)]$  in position  $x$  gives the cosine coefficients and sine coefficients which contain the following  $a_x$  and  $b_x$ , respectively.

$$a_x = A_1 \sin(\omega t + \theta_1) + A_2 \sin(\omega t + \theta_2) \quad (120)$$

$$b_x = -A_1 \cos(\omega t + \theta_1) + A_2 \cos(\omega t + \theta_2) \quad (121)$$

Fourier analyzing further the cosine and sine coefficients, we obtain the following four elements for the frequency  $\omega$  and wavenumber  $k$ .

$$c_{11} = A_1 \sin \theta_1 + A_2 \sin \theta_2 \quad (122)$$

$$c_{12} = A_1 \cos \theta_1 + A_2 \cos \theta_2 \quad (123)$$

$$c_{21} = -A_1 \cos \theta_1 + A_2 \cos \theta_2 \quad (124)$$

$$c_{22} = A_1 \sin \theta_1 - A_2 \sin \theta_2 \quad (125)$$

Solving (122-125) for  $A_1$  and  $A_2$ , we have

$$A_1 = \frac{1}{2} \sqrt{(-c_{12} - c_{21})^2 + (-c_{11} + c_{22})^2} \quad (126)$$

$$A_2 = \frac{1}{2} \sqrt{(-c_{12} + c_{21})^2 + (-c_{11} - c_{22})^2} \quad (127)$$

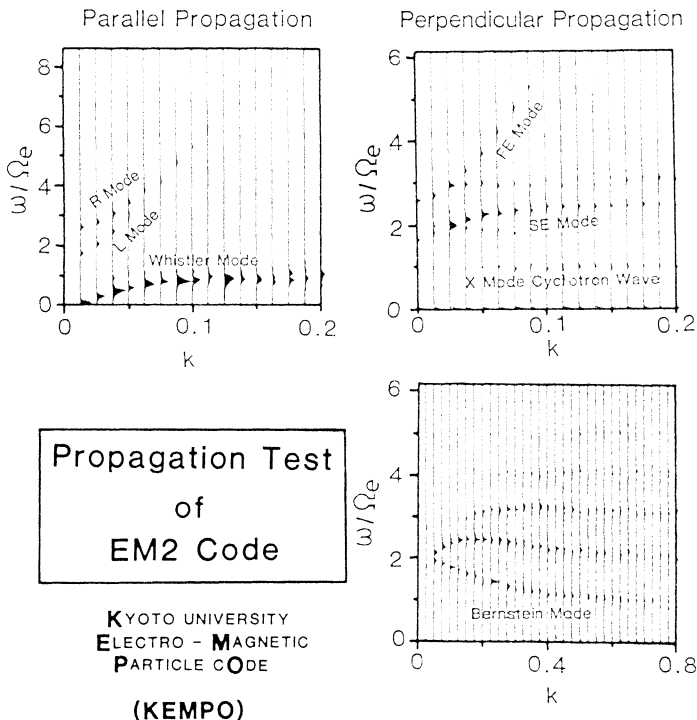


Figure 14.  $\omega$ - $k$  diagram of plasma dispersion relations observed in particle simulations by the KEMPO.

In the post-processor of the  $\omega$ - $k$  diagram, we calculate  $A_1$  and  $A_2$  for backward and forward traveling modes. In Figure 14 we show some of the outputs of the post processor. In this particular example, we applied the KEMPO to one dimensional problem with a model in which only thermal electrons are present initially. Out of thermal fluctuations of electrons, only electromagnetic as well as electrostatic waves satisfying the plasma dispersion are left over. Spectra shown in Figure 14 are summation of forward and backward propagation. The upper left panel shows spectra of the transverse magnetic field  $B_y$  in a case where the wavenumber vector  $k$  is parallel to the static magnetic field. We can recognize the R mode, L mode and whistler mode. The upper right panel shows spectra of the magnetic field  $B_z$  in the case of perpendicular propagation where the wavenumber vector is in the  $x$ -direction and the static magnetic field is in the  $y$ -direction. We see fast and slow extraordinary modes and  $x$  mode electromagnetic cyclotron waves. The lower right panel shows the electrostatic component  $E_x$  in the same case of perpendicular propagation. We see very clear Bernstein modes.

We have described the one-dimensional  $\omega$ - $k$  analysis where the wavenumber  $k$  is in the  $x$ -direction. Extension to the two-dimensional  $\omega$ -( $k_x$ ,  $k_y$ ) analysis is simple in algorithm, but it requires a large size of memory because the data to be analyzed become three-dimensional array [ $a(x, y, t)$ ].

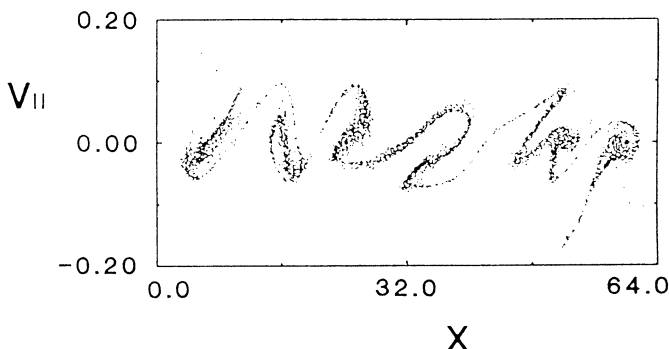


Figure 15. Phase space plot in the  $v_{||}$  -  $x$  plane.

#### 5.4 Miscellaneous Diagnoses

Other than diagnoses of energy and  $\omega$ - $k$  spectra, various analyses are needed depending on physical problems under consideration. However, most of them does not require any special techniques in data processing. They only depends graphic routines for a  $(x, y)$  axis plot, a contour map, a three-dimensional perspective plot, etc., which

are not directly related to nor inherent solely to particle simulations. Therefore, we briefly introduce examples of miscellaneous diagnoses.

### (1) Phase Space Plot

A typical diagnosis of particle simulations is a phase space plot of particles. Locations of particles at a certain time is plotted by dots in a two-dimensional phase space where two of five components ( $x$ ,  $y$ ,  $v_x$ ,  $v_y$  and  $v_z$ ) are selected. An example of the phase space plots in the  $v_{||}$ - $x$  plane is shown in Figure 15.

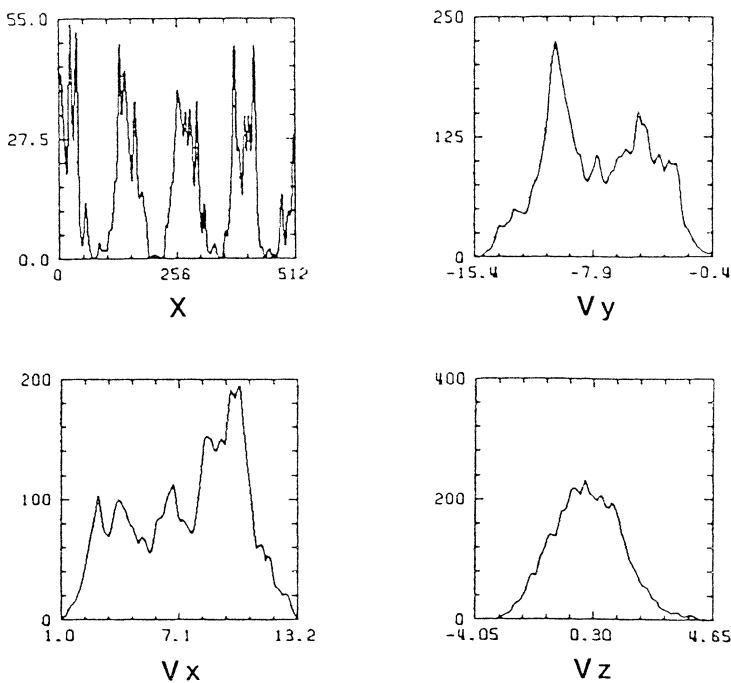


Figure 16. Particle distribution function in  $x$ ,  $v_x$ ,  $v_y$  and  $v_z$ .

### (2) Distribution Function

In the diagnostic routine in the KEMPO, distribution functions of particles in a simulation run are calculated and stored into a data file. Reading the data from the file, one of the post processors plots the distribution functions in  $x$ ,  $v_x$ ,  $v_y$  and  $v_z$  as shown in Figure 16. Another post processor plots a two-dimensional particle distribution in the  $x$ - $y$  plane using a three-dimensional perspective graphic routine as shown in Figure 17, which shows a hole formed in the plasma due to an electron beam injection.

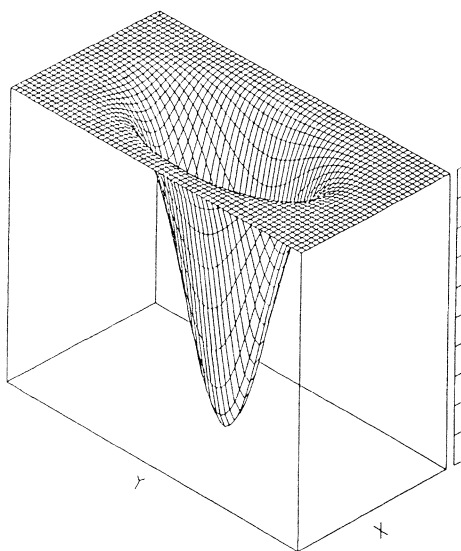


Figure 17. Particle distribution function in the  $x - y$  plane : a three-dimensional perspective plot.

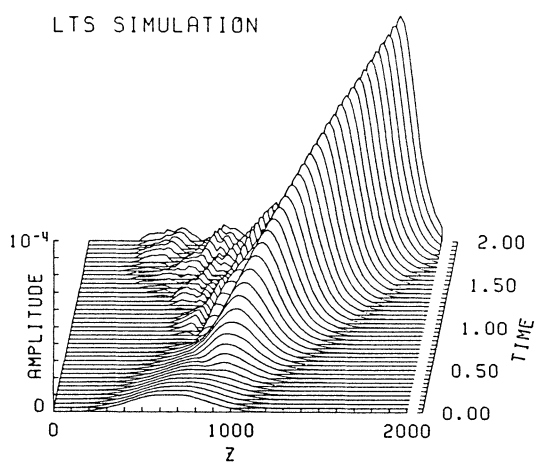


Figure 18. Spatial variation of wave amplitude and its time evolution.

### (3) Spatial Variation and Time Evolution

By plotting one-dimensional spatial variation of field quantities with a slight shift at each time, we can see time evolution of the spatial variations. In Figure 18 we plot an output of KULTS code where we can see propagation of a whistler pulse with its growth and damping.

### (4) Two-dimensional Vector Plot

Two-dimensional vector quantities defined in the x-y plane such as a current density ( $J_x, J_y$ ), or a electrostatic force ( $E_x, E_y$ ) are effectively indicated by arrows in the x-y plane. Intensities are indicated by the size of arrows. Figure 19 shows a flow pattern of current densities observed in a beam injection simulation by the KEMPO.

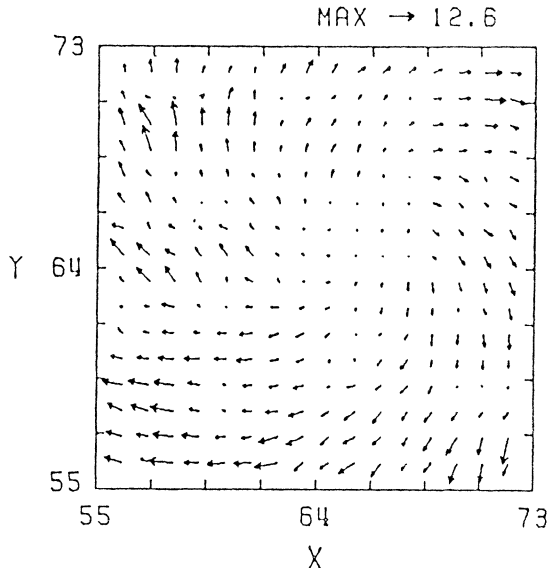


Figure 19. Two-dimensional vector plot : Flow pattern of current densities in x - y plane.

## 6. APPLICATION TO SPACE PLASMA WAVE PHENOMENA

The particle simulation codes developed at RASC such as the KEMPO and KULTS have so far been used to interpret nonlinear plasma dynamics associated with space wave phenomena and related particle events observed by space vehicles. In this section, we briefly describe three examples out of them.

Space observations are limited by two main reasons. First is due to limited power, volume and weight available to scientific payload in almost any space vehicles. Complicated and fancy measurements are therefore given up in most cases. This causes lack of information on detailed structures of field and particles blocking theoreticians to construct a satisfactory theory or scenario for the observed phenomenon. For example, very few simultaneous data of density of cold plasmas, velocity distribution functions of energetic particles and fields have been available from spacecraft. The other drawback of space vehicle observations is due to a fact that the observation is made only on a limited region in the vast area of space plasmas. Sometimes an interesting electromagnetic phenomenon is detected by wave receivers but not by particle detectors. This often means that the space vehicle missed a chance to pass the most interesting area where the corresponding wave-particle interaction takes place and picked up only the propagated wave effect.

Section 6.1 and 6.2 are examples of applications of the KEMPO to problems in which both electromagnetic and electrostatic waves play key roles in the wave-particle interactions. These examples are appropriate ones to demonstrate how computer simulations can provide detailed information which could never be obtained by spacecraft observations nor by analytic theories, compensating the first limitation of space observations. Section 6.3 is an example of simulation by the KULTS applied to whistler mode nonlinear wave-particle interactions in the inhomogeneous magnetic field. This is a good example to demonstrate the usefulness of the LTS code to handle a nonlinear interaction which takes place in a wide area of space over thousands of wavelengths along the inhomogeneous plasma medium such as that in the magnetospheric plasma, which is not observable as a whole by spacecraft either.

All examples shown in this section have already been published in journals so that only the background philosophy and motivation of each simulations are given together with a brief summary.

### 6.1 Hook-induced Electrostatic Bursts

This particular example is a particle simulation by the KEMPO on nonlinear wave-particle interactions involving obliquely propagating whistler mode wave and electrostatic waves. Reinleitner et al. [1982, 1983] discovered by ISEE satellite that strong electrostatic (ES) burst emissions are often associated with a coherent whistler mode chorus hook element, as shown in Figure 20, and that a high energy electron beam with an energy of the order of several hundred electron volts is always found at the time of occurrence of these ES bursts.

Motivated by the discovery, we started our particle simulation by the use of the KEMPO to shed some light into its physical mechanism [Matsumoto et al., 1984]. The KEMPO is useful to this kind of problems because both electromagnetic and electrostatic waves are

# ISEE Observation of Chorus-induced Electrostatic Burst

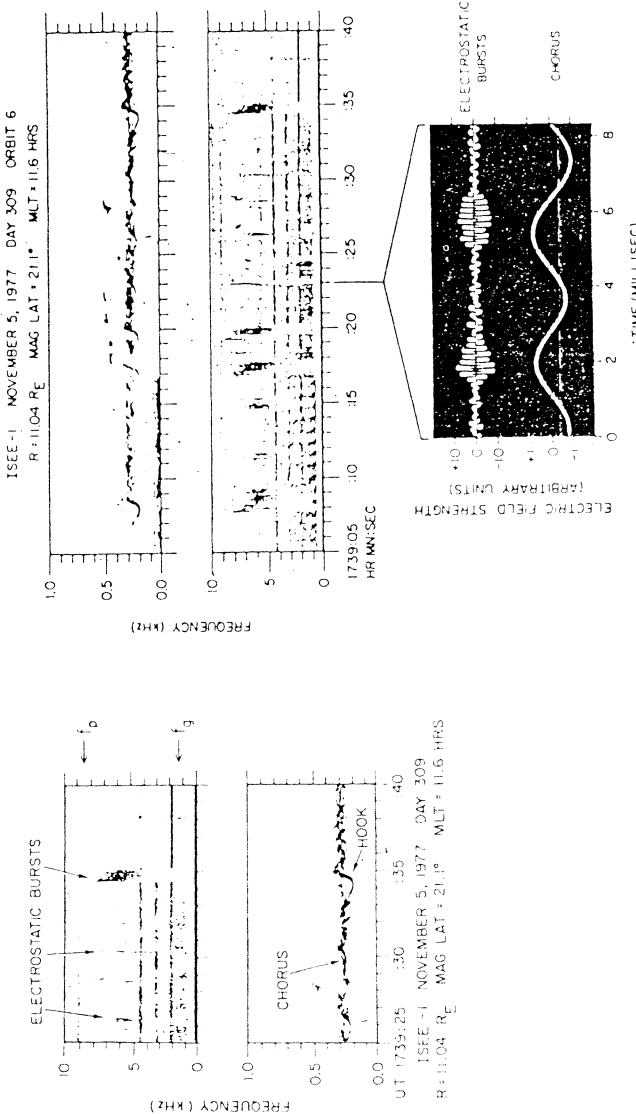
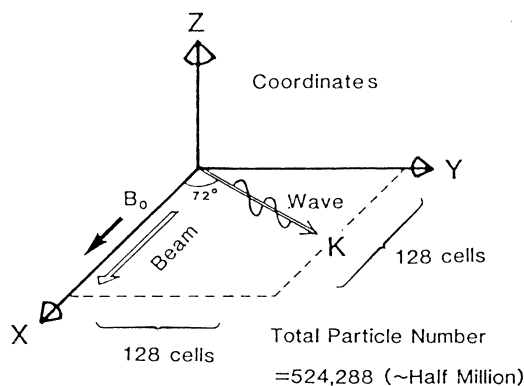


Figure 20. Observation data by ISEE satellite: Strong electrostatic (ES) burst emissions are associated with a coherent whistler mode chorus element.

automatically treated simultaneously. Two-and-a-half dimensional model was hired instead of easier one-and-a-half dimensional model because we need to know which kind of ES mode is preferentially excited by the chorus element as a result of interaction with enhanced population of high energy electrons, and to see which direction of the  $\mathbf{k}$  vector of the excited waves is to be as a result of the nonlinear interaction. Thus a model shown as Figure 21 was adopted.

### SIMULATION MODEL



### SIMULATION PARAMETERS

$\Pi_e=2$	$\omega=0.27$	$\Delta t=0.01$
$\Omega_e=1$	$\theta=72^\circ$	$\Delta r=1.0$
$N_b/N_a=10^{-2}$	$B_w/B_0=10^{-2}$	$\lambda_0=1.0$
$V_{th}=2.0$	$M_x=1$	
$c=50.0$	$M_y=3$	

Figure 21. Simulation model and parameters.

Prior to our simulation, we assumed that the ES bursts are produced by a coherent nonlinear interaction of a monochromatic whistler wave with resonant electrons in the enhanced bump in the tail in the velocity distribution function seen by ISEE at the time of the event. Therefore we carried out two different runs; one for a simple beam-wave interaction without a monochromatic whistler wave and the other with a monochromatic whistler wave. Like this example, to make

## K SPECTRUM

$\omega$ -Range = 0.0~2.4

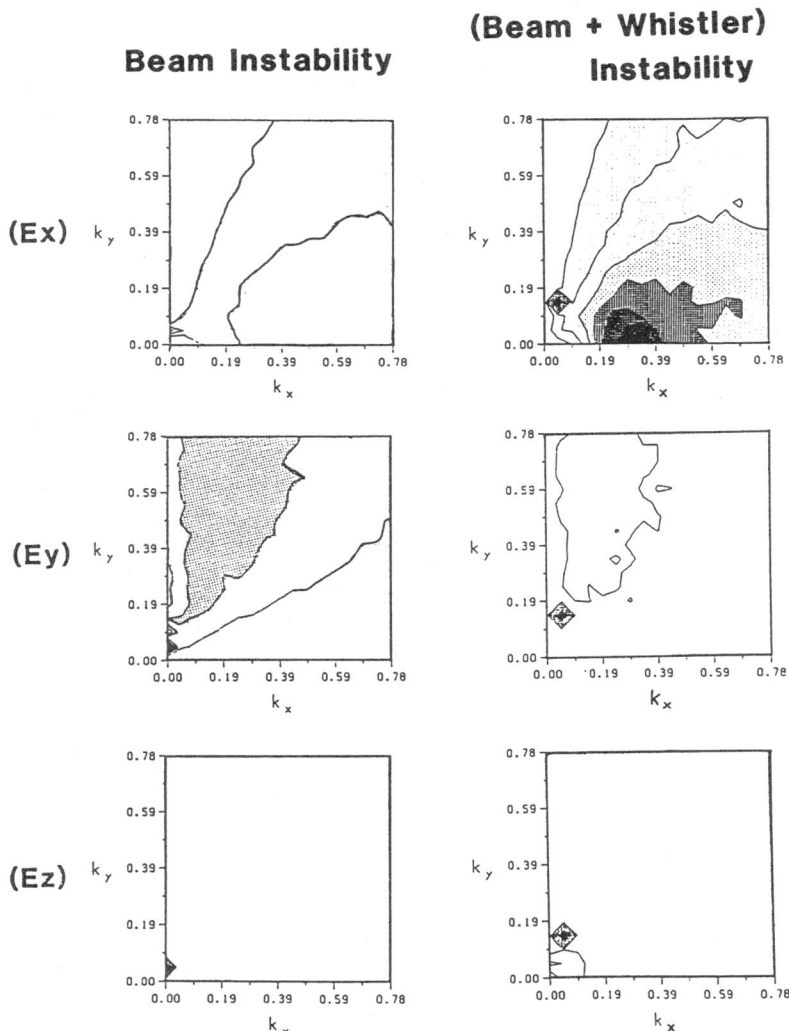


Figure 22. Spectrum of wavenumber  $k$  in  $k_x$ - $k_y$  plane : (a) Beam only, (b) Beam + Whistler

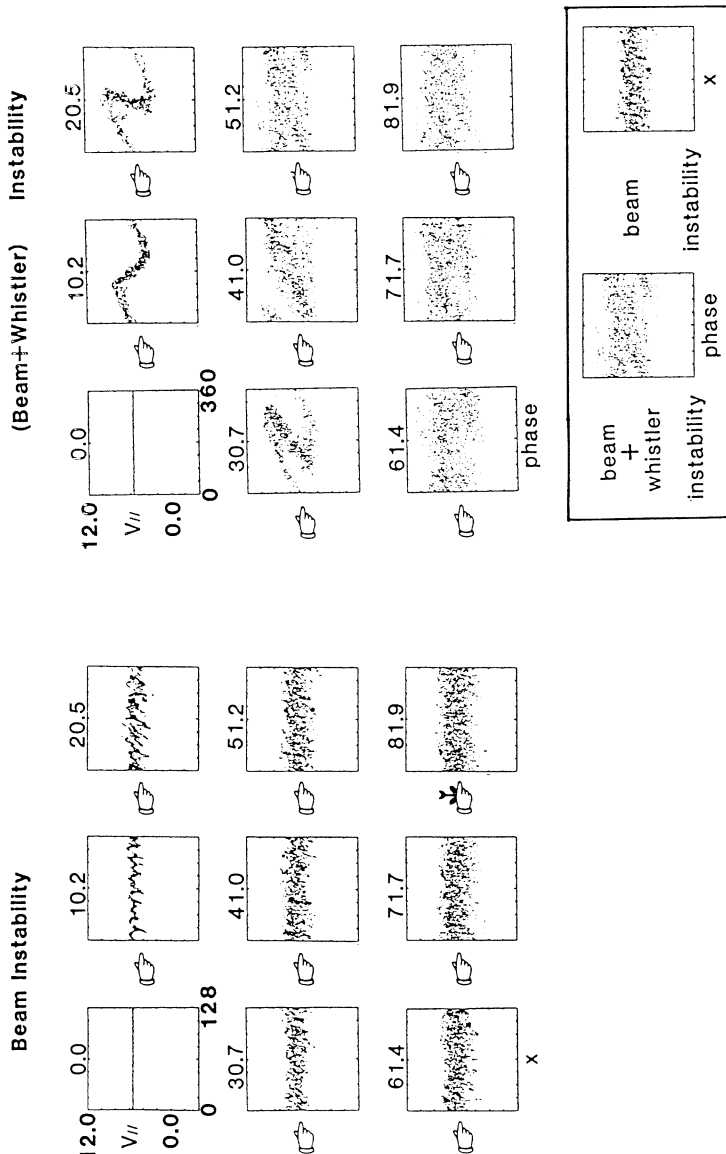


Figure 23. Phase space plot for beam electrons in  $V_{\parallel}$  - phase plane.  
 (a) Beam only, (a) Beam + Whistler

different numerical experiments by changing some key parameters or by eliminating or adding some elements participating in the interaction of interest is one of the advantages of computer simulations.

Such contrasting runs revealed the role of the coherent whistler wave. Figures 22 and 23 show comparisons of results of the two contrasting case A (beam only case) and case B (beam + whistler case) for a contour map of electric fields  $E_x$ ,  $E_y$  and  $E_z$  in  $k_{\parallel}$ - $k_{\perp}$  plane, and for time evolution of  $v_{\parallel}$ - $x$  phase diagrams. These diagnostic figures together with other diagnostic tools as described in Section 5 lead to the following conclusion.

"The generation mechanism of the electrostatic burst emissions are essentially a beam instability boosted under the action of the electrostatic component of the obliquely propagating whistler wave. The role of the whistler wave is to produce two beams via action of nonlinear trapping and subsequent detrapping process. One beam has higher velocity than the whistler phase velocity along the external magnetic field  $B_0$  (i.e., resonance velocity) and the other has lower one. The two beam jetting enhances the growth rate of the electrostatic waves propagating along  $B_0$ ."

## 6.2 Wave Excitation and Particle Acceleration by Artificial Electron Beam Injection

Active experiments in space plasmas have recently been carried out extensively to investigate dynamical nature of space plasmas. Principle of these active experiments is to give artificial perturbations to the plasma and then measure its response and reaction. As the perturbation is given locally (and strongly in most cases), the response is transient, strongly inhomogeneous and highly nonlinear. It is generally difficult to treat by analytic theories such transient phenomena with highly inhomogeneous and nonlinear nature. Computer simulations are very effective to such problems. We will show an example of application of the KEMPO to one of the active experiments.

Electron beam injection is one of the most frequently used methods in active experiments. We performed two computer simulations with two different models in order to give physical interpretation of the phenomena obtained in the SEPAC (Space Experiment with Particle ACcelerators) onboard the Space Shuttle/ Spacelab-1; one is with a one-and-two-half dimensional model taking the model plane normal to the electron beam, and the other is with a one-and half dimensional model taking the 1D axis perpendicular to the electron beam. In both models, the beam is assumed to be parallel to the external magnetic field  $B_0$  as the SEPAC electron gun launched the electron beam along  $B_0$ .

The first simulation with two-and-half dimensional model was performed mainly to investigate radiation of electromagnetic and electrostatic waves with  $k$  vector perpendicular to the beam and  $B_0$

## Excitation of O-mode Waves

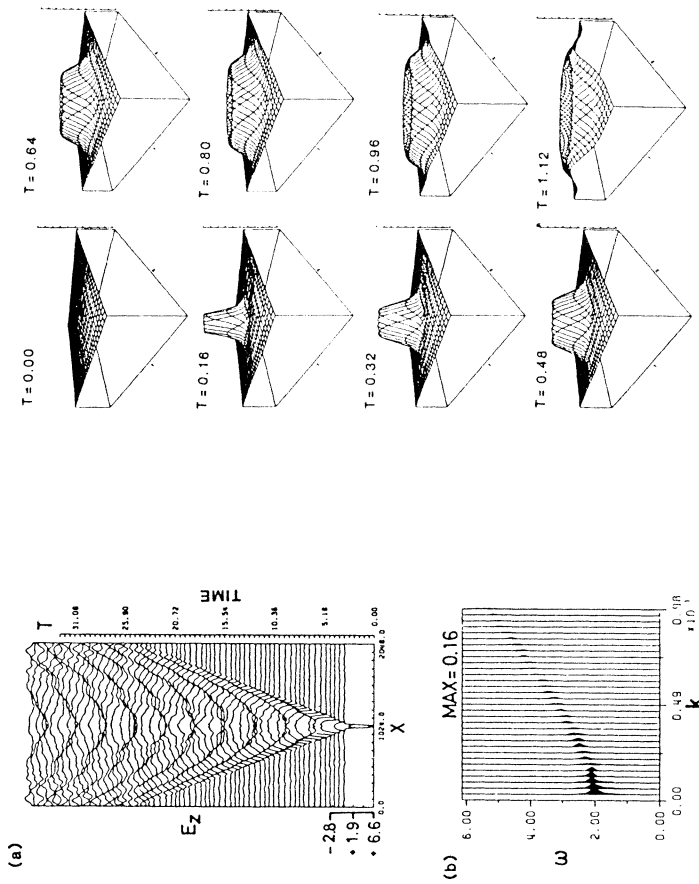


Figure 24. Excitation of O mode waves

direction [Omura and Matsumoto, 1984a]. Figures 24 and 25 are a part of the results showing the O-mode and X-mode wave radiation, respectively. In each figure, the time evolution of the wave amplitude (showing propagation effect), and  $\omega$ - $k$  diagram (compared with linear theory shown by a solid line in Figure 25) are given. In Figure 24 a three-dimensional display of the  $E_z$  component is shown as well, while time evolution of contour maps of densities of background and beam electrons are shown in Figure 25.

## Excitation of X-mode Waves

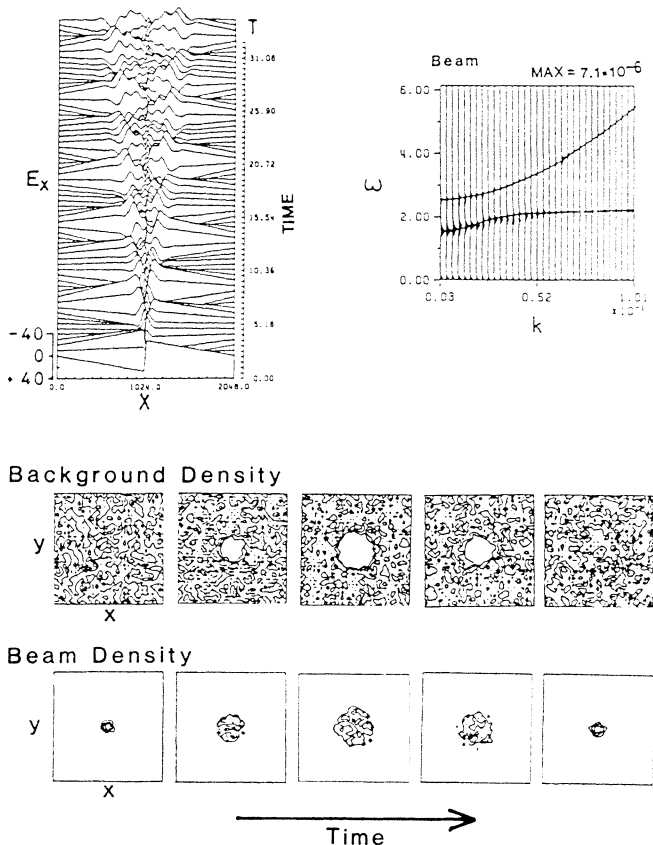


Figure 25. Excitation of X mode wave

It is expected before simulation that the O mode wave is radiated from the beam column and propagates in the radial direction as a result of a sudden injection of the beam current. However, in addition to the first impulsive radiation of the O mode electromagnetic wave, many pulses are launched from the beam successively as seen in the left upper panel and in the right 3D display of Figure 24. This comes from a fact that the beam current intensity is modulated by the change of the size of the beam column due to electrostatic oscillations.

Figure 25 shows that the hybrid mode oscillation of beam and plasma density is caused by excess charge injection in a localized area at the position of the beam and is a dominant source of the X mode radiation. The  $\omega$ - $k$  diagram indicates that the predominant mode is the slow extraordinary mode waves in the frequency range below the upper hybrid frequency ( $(\Omega_e^2 + \Omega_{ce}^2)^{1/2} \cong 2.25$ ). The lower panel shows that the background ionospheric plasma responds to the beam injection in such a manner that a variable-sized hole is created at the location of the beam.

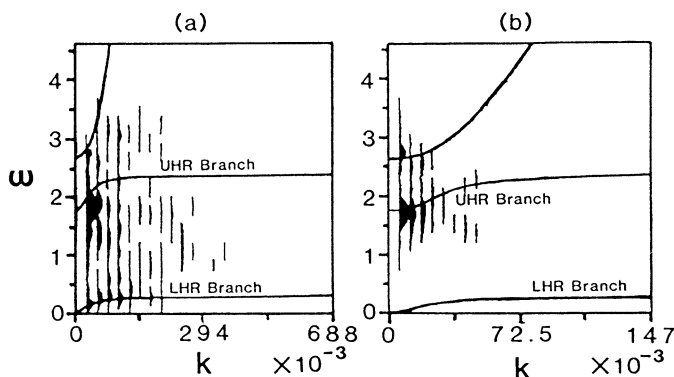


Figure 26.  $\omega$ - $k$  diagram : (a) wave spectra in the localized area in the vicinity of the beam, (b) wave spectra in the whole simulation region.

In the second simulation [Matsumoto and Fukuchi, 1984], ions are taken into account as a mobile constituent on top of background and beam electrons. In addition to the high frequency UHR waves on the UHR branch in the  $\omega$ - $k$  diagram as shown in Figure 26(b) which was made by FFT analysis from field data in the whole region in the simulation model, lower hybrid waves (LHR waves) are also excited in the vicinity of the beam location as seen in Figure 26(a) which is the  $\omega$ - $k$  diagram

## Excitation of LHR Waves and associated Particle Acceleration

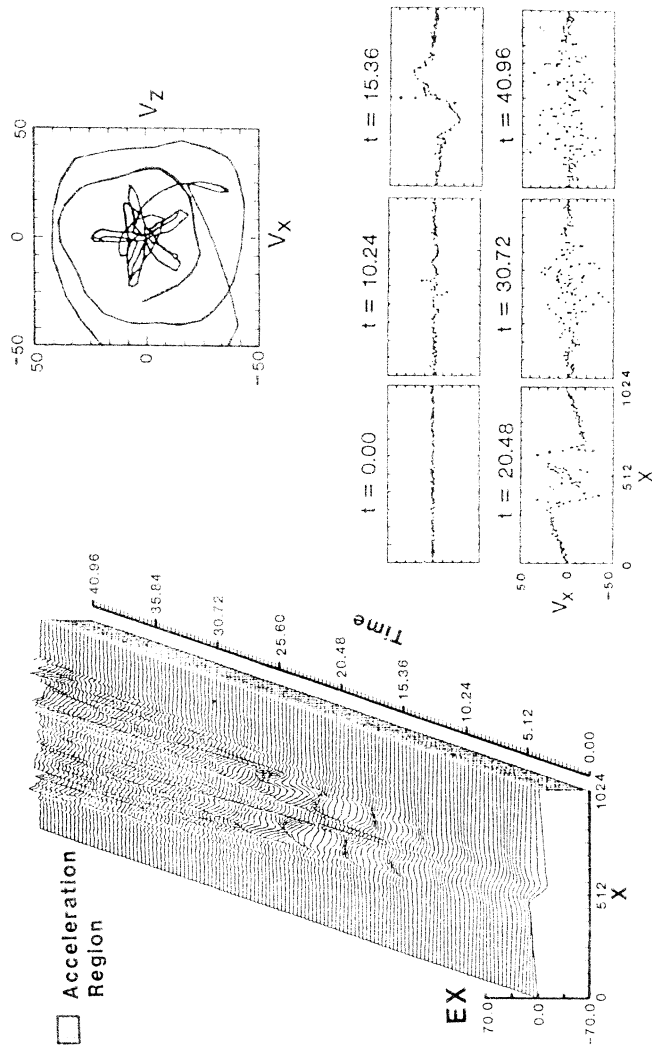


Figure 27. Excitation of LHR waves and associated particle acceleration

made from field data only from a localized area in the vicinity of the beam. Figure 27 shows the corresponding electric field structure of the LHR waves as a function of time (left panel) together with a time evolution of the  $V_x$ - $X$  phase diagram of background electrons (lower

right panels) and a typical orbit in the  $V_{\perp}$  plane of an accelerated electron. Ions start to move responding to the slowly-varying component of the electric field after  $t \sim 15$  which is about half of the LHR period under the simulation parameters. Therefore we can see the low frequency LHR waves with pulsive nature and with short wavelengths of the order of 100  $\lambda$  excited first in the vicinity of the beam location at the central area of the system, and then propagate outward at later time. Some of the background electrons are accelerated by the local Landau resonance with the LHR waves when its velocity component parallel to the direction of propagation of the LHR waves becomes close to their phase velocity. This result of simulation gave an interpretation to the SEPAC result that very high energy electrons with pitch angles more than 88 degrees are found in the vicinity of the Shuttle when the electron beam was injected.

It is possible to predict qualitatively some of expected responses to such artificial perturbations by analytic theories. However, most of the complicated responses can neither be predicted by analytic theories nor even be interpreted properly without assistance of computer simulations. It is easy to understand and interpret the simulation results and thereby corresponding experimental results in terms of fundamental elements of physics by making as detailed diagnoses as one desires. The reverse process, however, is hardly possible. Reader may recall the famous tale about Columbus's Egg in this regard. In other words, it is extremely difficult for theories without simulations to predict the response of the plasma to the active perturbations and even to give proper interpretations of the experimental data because the data set itself is far from complete and only a fractional reflection of the whole complicated physical processes. Japanese and Chinese (and probably some other countries') proverb says "GUNMOH-ZOH-NADERU" (which means many blinds surrounding an elephant guess wrong by touching only its fractional part without any knowledge of this animal). We might fall into pit-holes in interpreting plasma processes if we make our interpretation scenario without qualitative and quantitative investigation. Simulations are, of course, not almighty but at least can be a good guide for researchers.

### 6.3 Nonlinear Whistler Interaction

One of the unsolved open problems in space plasma physics is the generation mechanism of VLF triggered emissions. This section is devoted to demonstrate an application of the KULTS to the VLF emission problem. It is now widely recognized that the VLF triggered emissions are the manifestation of nonlinear whistler interaction in the inhomogeneous magnetic field structure. This means it is uneconomical and practically impossible to simulate the whole emission process by a full electromagnetic (EM) particle code such as the KEMPO because the interaction region is of length of thousands of wavelengths and is much longer than the grid size which is the order of the Debye length in such EM particle code. The LTS code is useful to such a problem

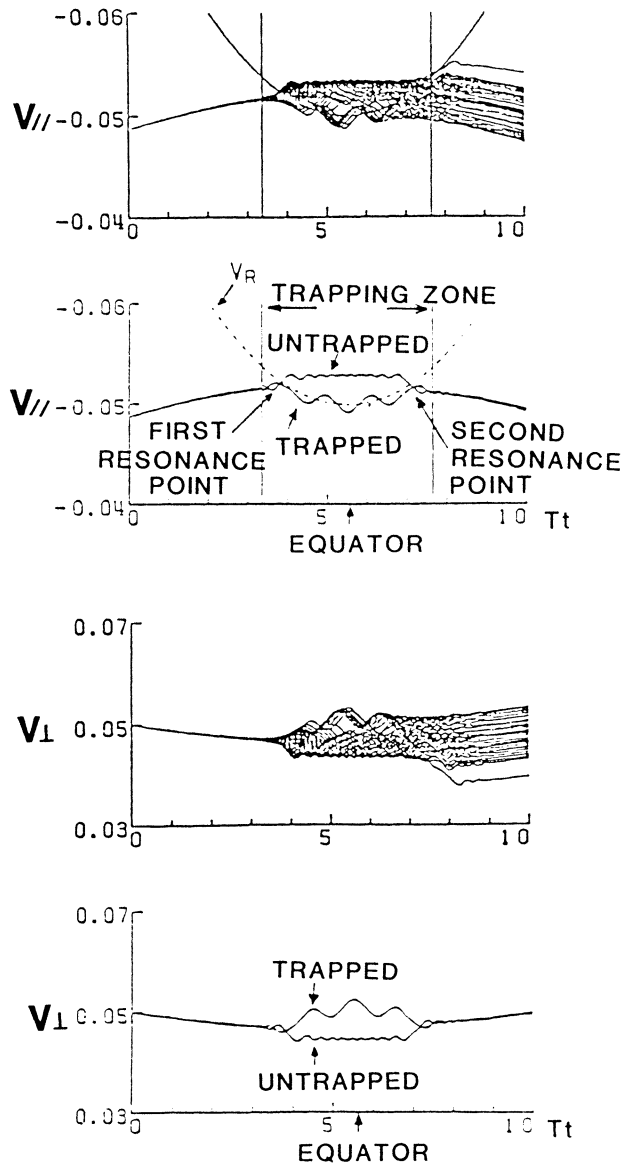


Figure 28. Trajectories of resonant electrons in a dipole magnetic field.

because the grid size can taken much larger than the Debye length as it does not solve the phase variation of the wave but solve only the slowly varying amplitude, frequency and wave number. The drawback of the LTS as a compensation of this gain is as follows.

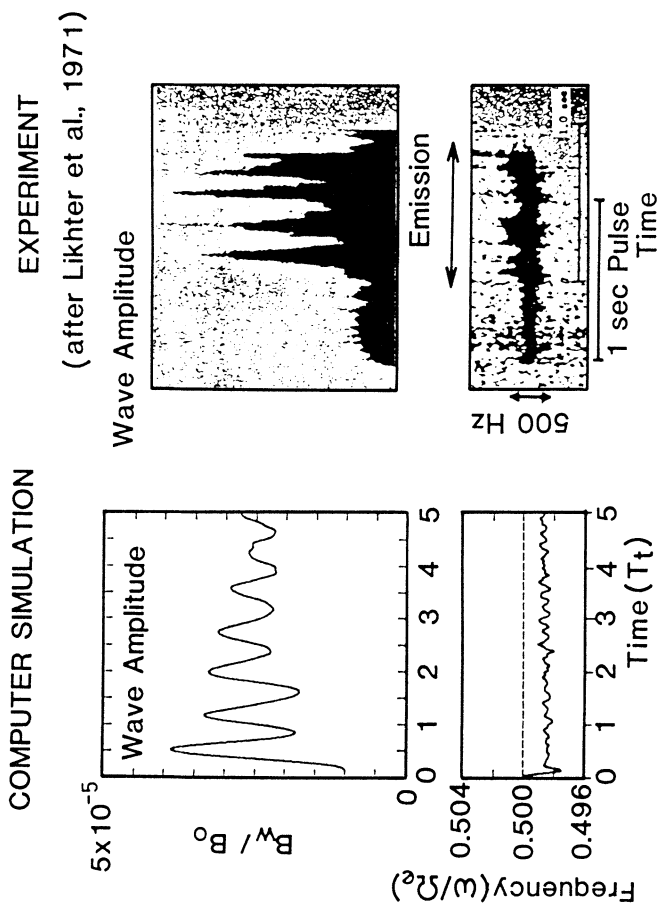


Figure 29. Comparison between simulation and experiment.

1. It can handle only one single wave mode and hence must neglect wave-wave couplings or competing process related to other wave modes.
2. Linear response of the background (non resonant) particles should be assumed. This means a highly nonlinear problem cannot be treated where the wave amplitude is such large as to drive the background plasma particles to nonlinear orbit.
3. The code is invalidated when the wave amplitude becomes zero or extremely small value.

The LTS code has often been used in coherent nonlinear whistler problems in disregard of these drawbacks [Rathmann et al., 1978; Vomvoridis et al., 1982; Omura and Matsumoto, 1982; Matsumoto and Omura, 1983; Omura and Matsumoto, 1984b].

Examples of the results of the KULTS simulations are shown in Figures 29, 30 and 31. Figure 28 shows orbits of resonant electrons in the velocity-vs-time plot. By this diagnosis we can clarify dynamical behavior of trapped and untrapped particles under the nonlinear force due to the wave and mirror force due to the inhomogeneous magnetic field. Figure 29 is an example of comparison between simulation and experiment. The characteristics of amplitude oscillation and associated small frequency variation are well reproduced in the simulation. The third example obtained by the KULTS simulation shown in Figure 30 is the time evolution of the wave amplitude of the triggering wave (TW) pulse and its frequency variation with time. Followed by the amplified TW, triggered emissions are clearly seen associated with a frequency variation as shown in the upper right panel. The last example in Figure 31 is the result of a run which examined the contribution of untrapped but resonant electrons to the wave growth in the inhomogeneous medium. In this particular example, we artificially input a special group of electrons which are not trapped by the wave in order to investigate the role of untrapped resonant electrons. The result shows that these electrons contribute to give energy to the wave leading to a large amplification at the interaction point around  $z \approx 1000$ . The bottom panel shows the locations of these particles in the phase diagram. Obviously, as intended, the particles move outside the eye-shaped trapping area in the phase-space. This kind of artificial setting of initial conditions is one of the advantages of simulation. One can extract one or few important factors among various competing processes, which in the real plasma is not separable, yielding clearer understanding of the roles of the selected element(s) in the interaction.

**LTS SIMULATION of ENCOUNTER INTERACTION  
in HOMOGENEOUS PLASMA**

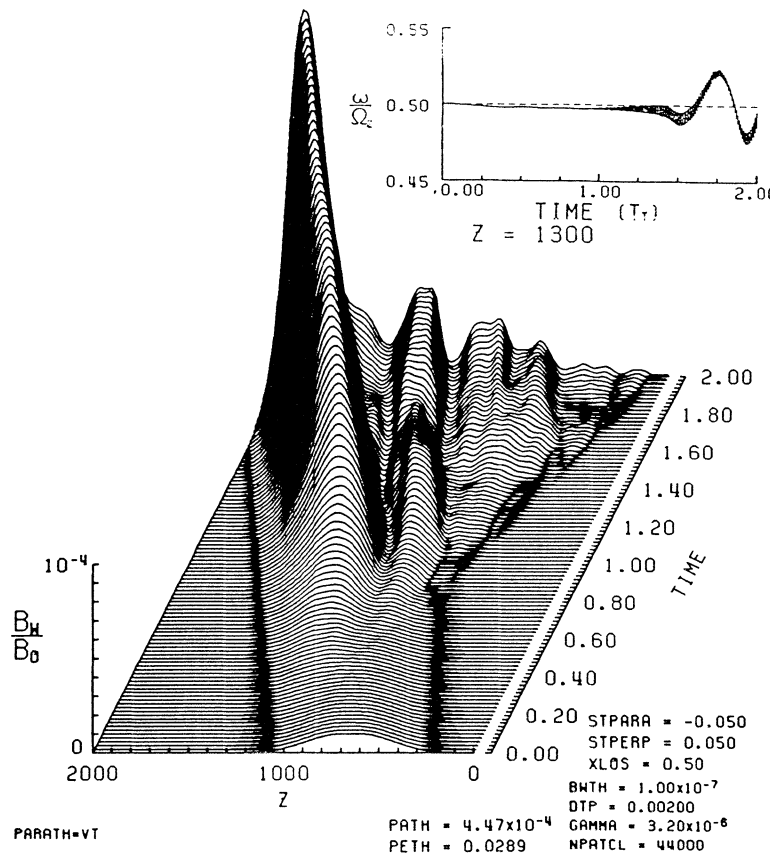
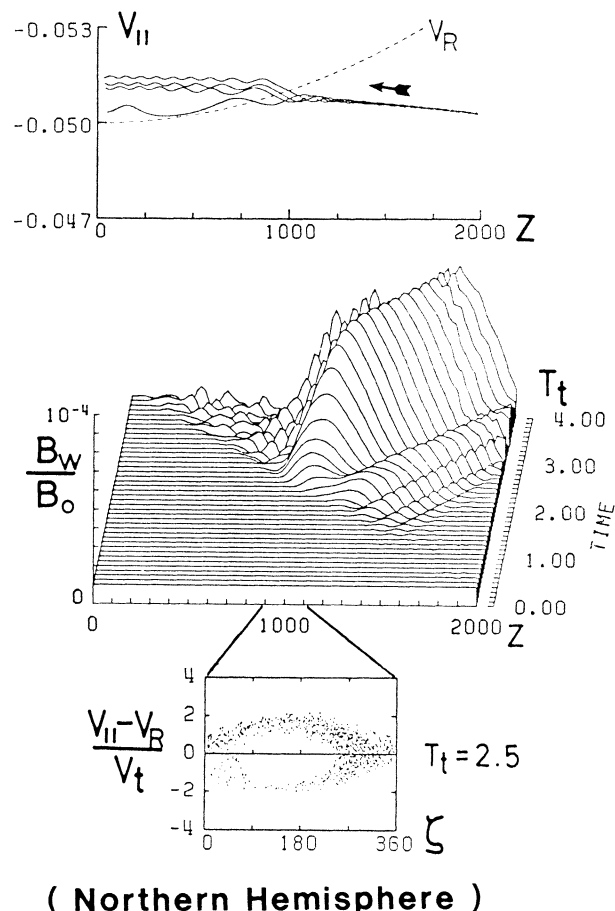


Figure 30. Time evolution of the wave amplitude of the triggering wave and its frequency variation with time.

### Growth by Untrapped Electrons



( Northern Hemisphere )

Figure 31. Wave growth due to the interaction with untrapped resonant electrons.

## 7. CONCLUDING REMARKS

In this article, we have given the outlines of the two kinds of particle simulation codes KEMPO and KULTS used at RASC for research of electromagnetic and electrostatic waves and of related wave-particle interactions together with examples of their application to space plasma phenomena. Some of the basic concept and techniques of electromagnetic simulations have also been described.

Readers are recommended to write their own code, not hiring or copying the others, because simulationists should be aware of the inherent limit of the code one uses, otherwise one may fall in a pitfall of erroneous conclusion by simply making a superficial comparison of the simulation results with observations. The needed attitude is to perform a simulation based on both sound physical insight into the physical process of interest and numerical techniques which one uses. We hope this article may be a help to the scientists and students who are going to make simulation studies in space plasma physics.

## ACKNOWLEDGEMENTS

We thank K. Miwa for typing the manuscript and students T. Yamada, T. Kimura, N. Komori, Y. Matsumoto, H. Tanaka, T. Tanaka, K. Inagaki and T. Ohashi at RASC for their help in preparing figures. Part of the simulations are supported by the Grant-in-Aid #56420016 of the Ministry of Education, Culture and Science, Japan.

## REFERENCES

- Abe, H., J. Miyamoto, and R. Itatani, J. Comput. Phys., 19, 134, 1975.  
Birdsall, C. K., and D. Fuss, J. Comput. Phys., 3, 494, 1969.  
Birdsall, C. K., and A. B. Langdon, Plasma Physics via Computer Simulation, McGraw-Hill, New York, in press, 1984.  
Boris, J. P., Proc. 4th Conf. on Numerical Simulation of Plasma, Stock 085100059, 3, U.S. Govt. Printing Office, Washington, D.C., 1970.  
Buneman, O., Phys. Rev., 115, 503, 1959.  
Buneman, O., J. Comput. Phys., 1, 517, 1967.  
Dawson, J. M., Phys. Fluids, 4, 869, 1961.  
Dawson, J. M., Methods Comput. Phys., 9, 1, 1970.  
Dysthe, K. B., J. Geophys. Res., 76, 6915, 1971.  
Hockney, R. W., Phys. Fluids, 9, 1826, 1966.  
Hockney, R. W., Methods Comput. Phys., 9, 135, 1970.  
Hockney, R. W., and J. W. Eastwood, Computer Simulation Using Particles, McGraw-Hill, New York, 1981.  
Kruer, W. L., M. Dawson, and B. Rosen, J. Comput. Phys., 13, 114, 1973.  
Langdon, A. B., and C. K. Birdsall, Phys. Fluids, 13, 2115, 1970.  
Langdon, A. B., and B. F. Lasinski, Methods Comput. Phys., 16, 327, 1976.

- Matsumoto, H., and Y. Omura, Geophys. Res. Lett., **10**, 607, 1983.  
Matsumoto, H., M. Ohashi, and Y. Omura, J. Geophys. Res., **89**, 3873, 1984.  
Matsumoto, H., and K. Fukuchi, Geophys. Res. Lett., in press, 1984.  
Morse, R. L., and C. W. Nielson, Phys. Fluids, **12**, 2418, 1969.  
Nielson, W.C., and H. R. Lewis, Methods Comput. Phys., **16**, 367, 1976.  
Okuda, H., and C. K. Birdsall, Phys. Fluids, **13**, 2123, 1970.  
Okuda, H., Proc. 4th Annu. Conf. on Numerical Simulation of Plasma, Office of Naval Research, Arlington, Va., 515, 1970.  
Okuda, H., and J. M. Dawson, Phys. Fluids, **16**, 408, 1973.  
Okuda, H., Computer Simulation of Space Plasma, 3, Terra Scientific Publishing Company, 1984.  
Omura, Y., and H. Matsumoto, J. Geophys. Res., **87**, 4435, 1982.  
Omura, Y., and H. Matsumoto, Radio Sci., **19**, 496, 1984a.  
Omura, Y., and H. Matsumoto, submitted to J. Geomag. Geoelectr., 1984b.  
Rathmann, C. E., J. L. Vomvoridis, and J. Denavit, J. Comput. Phys., **26**, 408, 1978.  
Reinleitner, L. A., D. A. Gurnett, and D. A. Gallagher, Nature, **295**, 46, 1982.  
Reinleitner, L. A., D. A. Gurnett, and T. E. Eastman, J. Geophys. Res., **88**, 3079, 1983.  
Vomvoridis, J. L., T. L. Crystal, and J. Denavit, J. Geophys. Res., **87**, 1473, 1982.